Revision 3

Word Count: 6,188 (Word count including references: 7,489)

Hydrothermal alteration of magmatic titanite: Implications for REE remobilization and the formation of ion-adsorption HREE deposits, South China

Yuzhou Feng[1, 2], Yuanming Pan[3], Bing Xiao[1, 2], Gaobin Chu[1, 2], Huayong Chen[1, 2, 4*]

[1]*Guangzhou Institute of Geochemistry, Chinese Academy of Sciences, Guangzhou 510640, China*

[2]*CAS Center for Excellence in Deep Earth Science, Guangzhou, 510640, China*

[3]*Department of Geological Sciences, University of Saskatchewan, Saskatoon, SK S7N 5E2, Canada*

[4]*Guangdong Provincial Key Laboratory of Mineral Physics and Materials, Guangzhou, 510640, China*

[*]Corresponding author: huayongchen@gig.ac.cn

Address: Guangzhou Institute of Geochemistry, Chinese Academy of Sciences, P.O. Box 1131, Tianhe District, Guangzhou 510640, Guangdong PRC

ABSTRACT

Ion-adsorption rare earth element (REE) deposits in South China are currently the main source of heavy rare earth elements (HREE). The Gucheng deposit in western Guangdong Province is one example of HREE mineralization hosted in

weathered coarse-grained biotite granites (CGBG). Titanite is a common accessory mineral in the CGBG and contains significant amounts of total REE (31,621 to 38,431 ppm), especially HREE (18,906 to 22,249 ppm). Titanite with a U-Pb age of 102.6 ± 1.9 Ma in the CGBG crystallized under relatively high temperatures (722-798 °C), high fH_2O, and high fO_2 conditions in the late magmatic stage, and has similar Nd isotopic compositions similar to the host CGBG: $^{143}Nd/^{144}Nd$ = 0.512062 to 0.512125 and εNd(t) = -7.4 to -8.6.

Back-scattered electron (BSE) imaging and TESCAN integrated mineral analyzer (TIMA) measurements show that titanite in the CGBG has been altered partly to fergusonite-(Y), rutile, calcite, quartz, and fluorite. The hydrothermal fluid responsible for titanite alteration was enriched in CO_3^{2-} and F, and was probably exsolved from the granitic magma. HREE released from the alteration of titanite were mostly scavenged by fergusonite-(Y) and rutile, which have been further replaced by gadolinite-(Y) and synchysite-(Ce). In addition, gadolinite-(Y) in the alteration assemblages exhibits further alteration and is characterized by elevated PO_4^{3-} and SO_4^{2-} contents in the altered parts. These results demonstrate that magmatic titanite in the CGBG underwent complex hydrothermal alteration, with a preferential accumulation of HREE in fergosnite-(Y) and gadolinite-(Y) in the alteration assemblages. Preferential HREE enrichments in magmatic titanite, and its alteration assemblages, are shown to play significant roles in the formation of the Gucheng HREE deposit.

Keywords: Titanite; Metasomatic alteration; REE-rich mineral; REE remobilization, Ion-adsorption deposit

INTRODUCTION

Currently, almost 35 % of China's total rare earth element (REE) production comes from ion-adsorption REE deposits clustered in South China (Sanematsu and Watanabe, 2016; Jowitt et al., 2017; Li et al., 2017a). This type of REE deposits also accounts for more than 80 % of the global HREE resources (Chi et al., 2012; Li et al., 2017a). The genesis of these deposits has resulted in large numbers of recent studies (Li et al., 2017a, 2019, 2020). These ion-adsorption REE deposits in South China are mostly hosted in the weathered crust of granites, where the parent granites have been proposed to have a great influence on ore formation (Bao and Zhao, 2003; Murakami and Ishihara, 2008; Li et al., 2017a, 2019, 2020). In addition, hydrothermal events commonly occur during the latest stage of granite crystallization, which may have played a key role during REE accumulation (Li et al., 2017a, 2019). During hydrothermal alteration, REE could have been leached from magmatic minerals, and subsequently scavenged by weathering-susceptible REE-bearing minerals (e.g., synchysite-(Ce) and gadolinite-(Y)) (Bern et al., 2017; Li et al., 2017a,b). As a result, magmatic minerals in granites typically show complex compositional textures (e.g., dissolution-reprecipitation) (Li et al., 2017a,b, 2019). These minerals can respond texturally and compositionally to changing physicochemical conditions and preserve a

wealth of information on hydrothermal processes and fluid compositions (Jamtveit, 1991; Pan et al., 1993; Van Hinsberg et al., 2010; Cao et al., 2015; Wen et al., 2020; Xiao et al., 2021).

Titanite ($CaTiSiO_5$) is a common accessory mineral in magmatic rocks. It can typically accommodate significant amounts of REEs and high field strength elements (HFSEs) (Pan and Fleet, 1991; Pan et al., 1993; Fu et al., 2016). Previous studies have shown that magmatic titanite is commonly enriched in LREE and can be partly replaced by hydrothermal fluids to form light rare earth element (LREE)-rich minerals (e.g., allanite, monazite) (Pan et al., 1993; Cao et al., 2015). The information behind this hydrothermal process can be recorded by textures and compositions of the titanite (Cao et al., 2015; Xu et al., 2015; Fu et al., 2016). Titanite can also accommodate considerable amounts of U and Th (with a high closure temperature of up to 700 °C; Fu et al., 2016). Thus U-Pb dating has a great potential on constraining magmatic events. In some ion-adsorption REE deposits, titanite is a particularly common accessory mineral in the granites (Li et al., 2017a,b). However, little attention has been paid regarding how magmatic titanite can be metasomatically altered and its effect on REE enrichment, especially heavy rare earth element (HREE) mineralization.

The Gucheng deposit is a newly discovered REE (HREE dominated) deposit in South China. It is HREE-dominated with ∑HREE oxides accounting for about 55 % of the total REE. Mineral exploration is ongoing in the Gucheng district, but resource estimates (i.e., tonnage and average REE grade) have yet to be publicly disclosed. The REE mineralization is hosted in the weathered crust of a coarse-grained biotite granite

(CGBG). Microscopic observations and mineral chemistry show that titanite in the CGBG is an important accessory mineral with abundant HREE. It exhibits very complicated replacement textures with variable HREE contents, which can be evaluated quantitatively to elucidate the role of hydrothermal alteration in the formation of HREE deposits. In this study, we present detailed documentation of the textures in the Gucheng titanite and its alteration products by scanning electron microscope (SEM) and TESCAN integrated mineral analyzer (TIMA) imaging. Integrating these textural relationships with electron microprobe analysis (EMPA) and laser-ablation inductively coupled plasma mass spectrometry (LA-ICP-MS) for the mineral chemistry, and laser-ablation multi-collector inductively coupled plasma mass spectrometry (LA-MC-ICP-MS) for U-Pb dating of titanite, we aim to evaluate the processes and roles of REE remobilization and transportation on HREE mineralization during titanite alteration.

GEOLOGIC SETTING

The Gucheng deposit, located approximately 179 km northwest of Guangzhou, Guangdong Province, South China, is situated in a world-class Fe-Cu-W-Sn-REE-Nb-Ta-U polymetallic mineralization region along the southern margin of Cathaysia (Fig. 1). This region was intruded by large volumes of granitic rocks during the Late Permian, Triassic, Jurassic, and Cretaceous (Li et al., 2017a). These granites were intruded into Proterozoic to Cambrian mudstones, sandstones, and shales, as well as

Devonian to Early Permian carbonate rocks (Li et al., 2017a; Zhao et al., 2017). Large numbers of regolith-hosted REE deposits have been discovered in the region, which can be subdivided into LREE- (e.g., Heling, Dingnan and Guposhan) and HREE-dominated types (e.g., Zudong and Dabu) (Li et al., 2017a). These REE deposits are temporally and spatially associated with the Middle Jurassic to Late Cretaceous granitic rocks.

The local stratigraphy at Gucheng consists of Early Devonian sedimentary units and Quaternary diluvium rocks (Fig. 2). The Early Devonian rocks are locally exposed in the north and dominated by sandstones and siltstones. The Gucheng REE deposit was formed by weathering of the Gucheng pluton, a granitic stock exposed over an area of 30 km^2, mainly including the coarse-grained biotite granite (CGBG), fine-grained biotite granite (FGBG), medium-grained biotite granite (MGBG), and a quartz diorite porphyry.

The CGBG is widely exposed in the Gucheng deposit with outcrops over 20 km^2. This type of granites has grain sizes of 2-10 mm in diameter, and consists mainly of K-feldspar (~20 modal %), plagioclase (~30 modal %), quartz (~32 modal %), biotite (~8 modal %), and hornblende (<5 modal %). Accessory minerals (<5 modal %) include allanite, titanite, apatite, zircon, magnetite, and fluorite. However, primary magmatic minerals in the CGBG commonly show varying degrees of late hydrothermal alteration: e.g. biotite being altered to chlorite, hornblende to titanite and chlorite, and plagioclase to muscovite (Feng et al., 2022). The FGBG, which is less common but is found in several drill holes, consists mainly of K-feldspar (~20

modal %), plagioclase (~32 modal %), quartz (~35 modal %), and biotite (~8 modal %), with grain sizes less than 1.0 mm. Accessory minerals (<5 modal %) include allanite, apatite, zircon, and Fe-Ti oxides (Feng et al., 2022). The MGBG, which is restricted to the southwestern part of the Gucheng deposit, is composed of mainly K-feldspar (~25 modal %), plagioclase (~32 modal %), and quartz (~35 modal %) as well as minor biotite (~3 modal %). Accessory minerals (< 5 modal %) include apatite and zircon. Near the surface, the CGBG, FGBG, and MGBG have all been intensely weathered, but the REE mineralization is restricted to the weathered crust of the CGBG. Geochemical data show that the CGBG has LREE, HREE, and LREE/HREE ratios of 143 to 211 (avg = 170), 17.4 to 30.6 (avg = 22.4), and 4.8 to 10.2 (avg = 8.0), respectively (Feng et al., 2022). Soil profiles at the Gucheng deposit vary from a few meters to > 30 m thick, with the economic ore bodies hosted mainly in the completely weathered zone containing enriched clay minerals.

SAMPLING AND ANALYTICAL METHODS

Five CGBG samples (ZK03-2, ZK03-4, ZK03-8, ZK03-9, and ZK06-1) were collected at depths of 41 m, 50 m, 61 m, and 70 m from the drill hole ZK03 and at 36 m from drill hole ZK06. These selected samples do not show any of the visible chemical weathering that is pervasive in the overlying REE mineralized soils. Polished thin sections of these samples were examined using optical microscopy and combined BSE and TIMA imaging to characterize mineralogical and textural

relationships, with an emphasis on the occurrence and texture of titanite. Specifically, several titanite grains exhibiting hydrothermal alteration have been characterized by *in situ* major and trace element analyses, whilst those without any obvious replacement were selected for Nd isotope and U-Pb dating. Compositions of other minerals (i.e., allanite, apatite, fergusonite, rutile and gadolinite) in the alteration assemblages associated with titanite were also determined by in situ major and trace element analyses.

BSE and TIMA imaging

The BSE imaging was carried out using a TESCAN MIRA3 field-emission scanning electron microscope (FE-SEM) at the Testing Center, Tuoyan Analytical Technology Co. Ltd., Guangzhou, China. After the samples were carbon-coated, BSE images were acquired under an acceleration voltage of 10 kV and a beam current of 15 nA. Mineral compositional mapping on the same MIRA3 FE-SEM was made using an acceleration voltage of 25 kV, a beam current of 8.24 nA, a working distance of 15 mm, and the pixel of the BSE images and the spacing between the points of energy dispersive spectrometry (EDS) analyses are 3.5 μm and 10.5 μm, respectively. The beam current and BSE signal intensity were calibrated automatically on a Pt Faraday cup. The EDS intensity was checked using a Mn standard. The samples were scanned using the TIMA liberation analysis module.

U-Pb dating, major and trace element analyses

Major and minor element compositional analyses of selected minerals were conducted using a JEOL JXA-8230 electron probe micro analyzer (EPMA) at the Sample Solution Co. Ltd., Wuhan, China. Operating conditions used for EPMA measurements of all standards and samples include 15 kV accelerating voltage, 20 nA beam current, 1 μm electron beam size, and 10 s counting time. To correct for matrix effects during EPMA, the ZAF correction was applied to transform the relative X-ray peak intensities into elemental weight compositions. The relative precisions of EPMA are < 2 % and < 5 %for major and minor elements, respectively.

Titanite U-Pb dating and trace element analysis of titanite, allanite, and apatite were conducted at the Key Laboratory of Mineralogy and Metallogeny, Guangzhou Institute of Geochemistry, the Chinese Academy of Sciences, using a laser ablation inductively coupled plasma mass spectrometry (LA-ICP-MS) (Resonetics RESOlution S-155 laser + Agilent 7900) with a spot size of 43 μm. This laser ablation system is equipped with a large sample cell (155 mm × 105 mm), which can host 20 epoxy sample mounts (having a diameter of 25.4 mm each). Its two-volume laser-ablation cell can wash out 99% of the signal within less than 1.5 s. A signal-smoothing and Hg-removing device was used in this laser ablation system to obtain smooth signals and reduce the Hg signals (Hu et al., 2014). Helium gas carrying the ablated sample aerosol was mixed with Ar carrier gas and N_2 as an additional di-atomic gas to enhance sensitivity in the ICP. Prior to analysis, the LA-ICP-MS system was optimized using the reference sample NIST610 ablated with a 29 μm spot size

and 5 μm/s scan speed to achieve maximum signal intensity and low oxide rates. Each analysis included approximately 20 to 30 s of background acquisition (from a gas blank) followed by 50 s of data acquisition from the sample. The MKED-1 titanite and the Mount McClure titanite were used as the primary and secondary standard, respectively, to calibrate the U-Pb age of the titanite (Spandler et al. 2016). The reference materials (NIST 610 + 612) were used as external calibration standards, while Ca was used as the internal standard to quantify elemental concentrations in the samples. The off-line selection and integration of the background and analyte signals, time-drift correction, and quantitative calibration, were performed using the software Iolite (Yan et al., 2020).

Nd isotope analyses

In situ Nd isotope analysis was performed on a Neptune Plus MC-ICP-MS (Thermo Fisher Scientific, Bremen, Germany) equipped with a Geolas HD excimer ArF laser ablation system (Coherent, Göttingen, Germany) at the Wuhan Sample Solution Analytical Technology Co., Ltd, Hubei, China. In the laser ablation system, He was used as the carrier gas within the ablation cell and was merged with Ar (makeup gas) after the ablation cell. Small amounts of nitrogen were added to the Ar makeup gas flow in order to improve the sensitivity of the Nd isotope detection (Xu et al. 2015). The spot diameters vary from 32 to 90 μm depending on the Nd signal intensity. The pulse frequency was changed from 4 to 10 Hz, but the laser fluence was

kept constant at ~8 J/cm2. A signal-smoothing device was used downstream from the sample cell to efficiently eliminate the short-term variation of the signal and remove Hg from the background and sample aerosol particles (Hu et al. 2014). The Neptune Plus is equipped with nine Faraday cups fitted with $10^{11}\Omega$ resistors. Isotopes ^{142}Nd, ^{143}Nd, ^{144}Nd, ^{145}Nd, ^{146}Nd, ^{147}Sm, ^{148}Nd, and ^{149}Sm were collected in Faraday cups using static mode. The mass discrimination factor for ^{143}Nd/^{144}Nd was determined using ^{146}Nd/^{144}Nd (0.7219) with the exponential law. The ^{149}Sm signal was used to correct the remaining ^{144}Sm interference on ^{144}Nd, using the ^{144}Sm/^{149}Sm ratio of 0.2301. The mass fractionation of ^{147}Sm/^{149}Sm was corrected by the ^{147}Sm/^{149}Sm normalization ratio of 1.08680 and the exponential law. All data reduction for the MC-ICP-MS analysis of Nd isotope ratios was conducted using "Iso-Compass" software (Zhang et al., 2020). Two natural titanite megacrysts, MKED1 and SP-Ttn-01, were used as the unknown samples in order to verify the accuracy of the calibration method for in situ Nd isotope analysis of the titanite. The chemical and Nd isotopic compositions of MKED1 have been reported by Spandler et al. (2016).

RESULTS

Textures of titanite and its alteration minerals

The titanite grains in the CGBG commonly occur either as replacement after hornblende or in the interstices of plagioclase, K-feldspar, and quartz, indicative of a relatively late crystallization after the major primary minerals. Titanite grains in the CGBG are euhedral to subhedral in shape, have a light brown color, range in size

mostly from 500 μm to 1.5 mm, and often contain inclusions of magnetite, zircon, and apatite (Fig. 3a-c). BSE images reveal that the titanite grains in the CGBG exhibit well developed zoning, with a typical pattern consisting of a light-colored core (titanite 1) and a dark rim (titanite 2) separated by a sharp boundary (Fig. 3b). Moreover, these primary titanite grains (titanite 1 and 2) are commonly partly replaced by the formation of an altered zone (titanite 3; Fig. 3b). In some cases, titanite grains have been almost completely pseudomorphed by an alteration assemblage consisting of rutile, quartz, calcite, and fergusonite-(Y) (Fig. 3d-g).

The allanite grains in the CGBG, which commonly occur in the interstices of plagioclase, K-feldspar and quartz, are euhedral to subhedral prisms of 300 μm to 1.0 mm long. BSE images reveal that the original allanite (allanite 1) grains are commonly replaced with an altered rim (allanite 2; Fig. 3h).

Fergusonite-(Y), with grain sizes less than 80 μm (Fig. 3e), is an important HREE-bearing alteration mineral associated with titanite, and often shows further alteration to gadolinite-(Y). The unaltered fergusonite 1 and altered fergusonite 2 are readily distinguished in BSE images, with the latter being darker with abundant porosities (Fig. 3i).

Similarly, rutile in the titanite alteration assemblage has euhedral to subhedral shapes with grain sizes from 50 to 100 μm (Fig. 3d-g). It shows well developed growth zoning in the BSE images (Fig. 3j-k). The rutile grains also commonly show further alteration to gadolinite-(Y) and, in a few cases, synchysite-(Ce) along the grain boundaries or in voids (Fig. 3j-k).

Gadolinite-(Y) grains are subhedral or anhedral with grain sizes of 10 to 50 μm (Fig. 3e and g). Similar to fergusonite-(Y), the gadolinite-(Y) grains commonly show varying degrees of hydrothermal alteration and can be subdivided into less altered (gadolinite 1) and more altered (gadolinite 2), with the latter being darker with more abundant porosities than the former under BSE imaging (Fig. 3l). Synchysite-(Ce) grains are irregular in shape with sizes less than 2 μm in diameter (Fig. 3k).

Chemical compositions of REE-bearing minerals

EPMA major and trace element compositions in titanite from the Gucheng CGBG are listed in Supplementary Appendix 1 and illustrated in Figure 4. Of the three types of titanite, titanite 1 contains higher TiO_2 (28.7 to 30.4 wt%), Al_2O_3 (2.3 to 3.7 wt%), Fe_2O_3T (3.6 to 4.5 wt%), Y (36,080 to 44,318 ppm), Nb (5,037 to 13,729 ppm), Zr (621 to 1,543 ppm), Hf (250 to 619 ppm), and Ta (2,950 to 10,864 ppm), with lower SiO_2 and CaO than titanite 2 and 3 (Fig. 4a-b). REE are also enriched in titanite I (∑REE = 31,621 to 38,431 ppm), but decrease sharply in titanite 2 (∑REE = 13,639 to 16,075 ppm) and titanite 3 (∑REE = 9,100 to 20,633 ppm). In the chondrite-normalized REE patterns, titanite 1 is characterized by a slight HREE enrichment and a pronounced negative Eu anomaly (Fig. 4c). Titanite 2 and 3 are also characterized by slight LREE enrichments and pronounced negative Eu anomalies (Fig. 4c). LA-ICP-MS mapping confirm a significant decrease of HREE from titanite 1 to titanite 2 and 3 (Fig. 4d-l).

EPMA major and minor element compositions in fergusonite-(Y) from the Gucheng CGBG are listed in Table 1 and illustrated in Figure 5. Of the two types of fergusonite-(Y), fergusonite 1 has higher Y_2O_3 (30.1 to 30.8 wt%) and WO_3 (8.8 to 9.2 wt%) contents as well as lower Nb_2O_5 (32.8 to 34.6 wt%), SiO_2 (< 0.01 wt%), CaO (0.3 to 1.1 wt%), ThO_2 (< 0.01 to 0.1 wt%), UO_2 (0.5 to 0.8 wt%), and F contents (< 0.01 wt%) than fergusonite 2 (Table 2; Fig. 5a). Both fergusonite 1 and 2 contain significant amounts of REE (except for Eu), of which fergusonite 1 contains lower LREE but higher HREE than the fergusonite 2 (Fig. 5b). EPMA mapping also shows a decrease of HREE and an increase of LREE from fergusonite 1 to fergusonite 2 (Fig. 5c-k).

Rutile has TiO_2, SiO_2, FeO, CaO, WO_3, Nb_2O_5, Ta_2O_5, and SnO_2 contents of 87.2 to 97.2 wt%, 0.01 to 2.1 wt%, 0.7 to 4.1 wt%, 0.03 to 0.6 wt%, < 0.01 to 4.5 wt%, 0.2 to 2.7 wt%, < 0.01 to 1.1 wt%, and < 0.01 to 1.4 wt%, respectively (Table 2). Gadolinite 1 contains higher TiO_2 (0.5 to 1.1 wt%), FeO (6.7 to 9.1 wt%) and Y_2O_3 contents (29.2 to 30.1 wt%) as well as lower SiO_2 (25.0 to 26.2 wt%), Al_2O_3 (< 0.01 wt%), CaO (1.9 to 3.6wt%), P_2O_5 (< 0.01 wt%), and SO_3 contents (< 0.01 wt%) than gadolinite 2 (Table 3; Fig. 6a). Both gadolinite 1 and 2 contain significant amounts of REE (except for Eu), but gadolinite 1 contains lower LREE and higher HREE (except for Tm) than gadolinite 2 (Fig. 6b). EPMA mapping also shows a decrease of HREE but an increase of LREE from gadolinite 1 to gadolinite 2 (Fig. 6c-h).

The REE compositions of allanite and apatite, determined by LA-ICP-MS, are given in Table 4 and Figure 7. The primary magmatic allanite (allanite 1) of the

CGBG is characterized by a LREE enrichment (Fig. 7a) with LREE, HREE and LREE/HREE of 195,744 to 211,588 ppm (avg. 203,200 ppm), 2,365 to 5,059 ppm (avg. 3,815 ppm), and 41 to 84 (avg. 57), respectively. The altered magmatic allanite-(Ce) (allanite 2) has higher HREE (4,485 to 8,497 ppm; avg. 6,511 ppm) but lower LREE (140,939 to 164,769 ppm; avg. 156,584 ppm) and LREE/HREE (19 to 34; avg. 26) than those of allanite 1. The magmatic apatite of the CGBG is also characterized by a LREE enrichment (Fig. 7b) and has LREE, HREE, and LREE/HREE of 3,816 to 7,997 ppm (avg. 6,671 ppm), 799 to 1323 ppm (avg. 990 ppm), and 4 to 10 (avg. 7), respectively.

U-Pb geochronology and Nd isotope composition of titanite

A total of 50 laser ablation spots from 50 titanite grains without obvious late hydrothermal alteration (i.e., only titanite 1 and 2) have been selected for U-Pb geochronology (Supplementary Appendix 2). These define a regression line on the Tera-Wasserburg plot with a lower intercept age of 102.6 ± 1.9 Ma (mean square weighted deviation or MSWD = 0.92; n = 50; Fig. 8).

Table 5 shows that titanite 1 and 2 in the CGBG have similar Nd isotopic compositions with a narrow range of $(^{143}Nd/^{144}Nd)_i$ values from 0.512062 to 0.512125, corresponding to εNd(t) and two-stage Nd model ages (T_{2DM}) values of -7.4 to -8.6 and 1538 to 1610 Ma, respectively (Fig. 9).

DISCUSSION

Elemental substitution mechanism and origin of titanite at Gucheng

The EPMA data calculated on the basis of 5 oxygen atoms (Supplementary Appendix 1) show that titanite 1, 2, and 3 all have significant Ca deficiencies at the Ca site (≥ 0.03 apfu). Moreover, the Ca contents of titanite 1, 2, and 3 collectively show a negative correlation with both LREE and HREE (Fig. 10a-b), indicating a substitution of Ca^{2+} by REE^{3+} (Pan et al., 1993; Cao et al., 2015; Fu et al., 2016). Linear correlations are also observed between Ti and (Al + Fe) in all three types of titanite (Fig. 10c), suggesting replacement of Ti^{4+} by Al^{3+} and Fe^{3+}. These results collectively suggest the charge-balanced coupled substitution: $REE^{3+} + (Al^{3+},Fe^{3+}) = Ca^{2+} + Ti^{4+}$.

In addition, titanite 1, 2 and 3 all contain detectable F contents (0.04 to 0.10 apfu), which may indicate a substitution of O^{2-} by F^{-} at the O site, as part of another charge-coupled substitution: $(Al^{3+},Fe^{3+}) + F^{-} = Ti^{4+} + O^{2-}$. This charge-coupled substitution leads to a hypotherical endmember $Ca(Al,Fe^{3+})O_4F$. The maximum proportions of this hypothetical end-member in titanite 1, 2 and 3, represented by the (Al+Fe)/(Al+Fe+Ti) molar ratio, are 24 mol%, 16 mol% and 17 mol%, respectively.

Other notable minor elements in the three types of titanite from the CGBG are Nb and Zr, which collectively also show a negative correlation with Ti (Fig. 10d), indicative of their locations at the Ti site involving charge-coupled (Nb^{5+}) and isovalent (Zr^{4+}) substitutions for Ti^{4+} (Chakhmouradian and Zaitsev, 2002,

Chakhmouradian, 2004). In contrast, deviations from unity at the Si site in all three types of titanite are invariably ≤ 0.02 apfu, suggesting negligible substitutions at this site.

At Gucheng, titanite 1 and 2 commonly exhibit both core-rim and sectorial zoning patterns that have been reported in many other magmatic titanites (Pan et al., 1993; Cao et al., 2015; Chakhmouradian and Zaitsev, 2002, Chakhmouradian, 2004; Hayden et al., 2008). They have similar Al (0.12 to 0.16 apfu and 0.08 to 0.10 apfu, respectively) and Fe (0.10 to 0.12 apfu and 0.07 to 0.08 apfu, respectively) and low Al/Fe ratios (1.02 to 1.55 and 1.23 to 1.40, respectively), which are characteristic of magmatic titanite in granites (Aleinikoff et al., 2002). In addition, titanite 1 and 2 have high REE, HFSE contents, and obviously negative Eu anomalies with relatively flat HREE patterns (Fig. 4c), which are also consistent with a magmatic origin (Xie et al., 2010; Gao et al., 2012; Cao et al., 2015). Moreover, the LA-ICP-MS U-Pb age of titanite (102.6 ± 1.9 Ma; Fig. 8) is within the analytical uncertainty of that from zircon (104 ± 1 Ma) (Feng et al., 2022). It has similar Nd isotopic compositions with the host CGBG (Fig. 9). All of these results indicate that titanite 1 and 2 in the CGBG have a magmatic origin, although textural evidence suggests its crystallization immediately after major minerals such as K-feldspar, plagioclase, quartz and hornblende (Fig. 3a-c).

The occurrences of magmatic titanite as replacement after hornblende and biotite (Fig. 3c) at Gucheng are similar to those discussed by Broska et al. (2007): i.e. breakdown of hornblende, biotite, plagioclase, and titanomagnetite resulting in a high

Ca and Ti activity environment for the formation of titanite during late magmatic crystallization. Thermodynamic calculations by Broska et al. (2007) suggested that these replacement reactions for the formation of titanite require a high fH_2O environment with relatively oxidizing conditions (see also Harlov et al., 2006). The water-rich and relatively oxidizing conditions for the formation of titanite at Gucheng are indicated by the replacement of primary Fe^{2+}-rich hornblende and biotite by more hydrous assemblages of chlorite with Fe^{3+}-rich allanite, epidote, and titanite. The Zr contents in titanite 1 and 2, using the pressure-dependent Zr-in-titanite geothermometer of Hayden et al. (2008), yield formation temperatures of 743-798 °C and 722-730 °C, respectively.

Titanite alteration process and REE remobilization

A salient feature of titanite at Gucheng is the pervasive replacement by secondary minerals (rutile, fergusonite-(Y), gadolinite-(Y), synchysite-(Ce), calcite and quartz) (Fig. 3e and g). Similar replacement textures have been reported for many other occurrences of magmatic titanite (Pan et al., 1993; Broska et al., 2007; Cao et al., 2015). The leaching and partial dissolution processes of titanite at Gucheng can be represented by the following reaction:

$$\text{Titanite} + CO_3^{2-} + F^- \rightarrow \text{rutile} + \text{calcite} + \text{quartz} + \text{REE-rich minerals.} \qquad (1)$$

Here, the release of REE from the partial or complete dissolution of titanite can be expressed as:

$(Ca_{1-x},REE_x)(Ti,Al,Fe)SiO_5 + (x-y)Ca \rightarrow (Ca_{1-y},REE_y)(Ti,Al,Fe)SiO_5 + (x-y)REE$, where $x > y$. (2)

Similar Al and Fe contents as well as similar chondrite-normalized REE patterns (i.e., pronounced negative Eu anomalies and relatively flat HREE) between titanite 2 (magmatic) and 3 (altered) (Fig. 4c) indicate that the hydrothermal fluid responsible for titanite alteration was most likely exsolved from the same magma as the CGBG. The common occurrences of calcite and fluorite in the alteration assemblages suggest that this magmatic-hydrothermal fluid was rich in CO_3^{2-} and F^-. Similarly, magmatic-hydrothermal fluids enriched in CO_3^{2-} and F^- have been proposed to be responsible for the formation of many other ion-adsorption REE deposits, where the CO_3^{2-} and F^- may be essentially derived from slab-derived aqueous fluids (Xu et al., 2017; Li et al., 2017a), and hence may represent an important factor promoting REE remobilization.

Mass-balance calculations on the occurrences of titanite pseudomorphs, consisting of rutile, calcite, quartz, and fergusonite-(Y) (Fig. 3e), show that the REE released from the alteration of titanite 1 and/or titanite 2 can be largely accommodated in fergusonite-(Y). However, the ratios of the average Lu contents in titanite 1 and 2 to the Lu contents in fergusonite 1 are 1/16 and 1/81, respectively (Fig. 11). These values are even higher than the volume proportion of fergusonite 1 in the whole titanite grain (1/118), which is calculated on the basis of the ratio of the area of all fergusonite-(Y) grains relative to the titanite grain on a plane (Fig. 3e). Similarly, all other REE in fergusonite 1 increase systematically with decreasing atomic number than their respective amounts in the titanite 1 and 2 precursors (Fig. 11). These results

demonstrate that some HREE and large amounts of LREE must have been leached away from the alteration assemblages by hydrothermal fluids (Pan et al., 1993). This titanite dissolution process results in significant fractionation between LREE and HREE, with HREE being preferentially enriched in fergusonite-(Y) from the alteration assemblages.

Rutile altered from titanite contains relatively high concentrations of Nb (0.13 to 2.66 wt.%), Ta (0.07 to 1.14 wt.%), and W (1.01 to 4.54 wt.%), which are generally insoluble in hydrothermal fluids (Wen et al., 2020). These elements in rutile can also be readily accounted for by the dissolution of magmatic titanite. Rutile at Gucheng has been further altered to gadolinite-(Y) and, occasionally, synchysite-(Ce) (Fig. 3j-k). Similarly, fergusonite-(Y) in the alteration assemblages often show further alteration to gadolinite-(Y), with additional enrichment in HREE (Dy, Ho, Er, Yb and Lu) but depeletion in LREE (La, Ce, Pr and Nd) as well as Nb, Th, U and F in the latter (Fig. 5 and 11). A possible process for the replacement of rutile and fergusonite-(Y) is that they were altered by the same fluid at the same time. Another possibility is that one of these two minerals was altered first by a fluid that was reactive with it but not reactive with the other one, and the other one was altered later by a different fluid that was reactive with it but not reactive with the first one. The first possibility is more likely because these two minerals often occur in close associations and would be both in the vicinity of the same fluid. Unfortunately, proof of either possibility by LA-ICP-MS dating is not feasible due to the fine-grained nature of the alteration products.

The alteration of rutile to synchysite-(Ce) suggests that this hydrothermal fluid

also contained F and CO_3^{2-}, similar to those responsible for the alteration of the magmatic titanite and allanite. However, textural relationships (Fig. 3) clearly show that rutile and fergusonite-(Y) are alteration products of titanite, suggesting two separate alteration events. We tentatively attribute the alteration of rutile and ferdusonite-(Y) to a late hydrothermal event associated with the FGBG with a zircon U-Pb age of 98.9 ± 0.7 Ma (Feng et al., 2022). Therefore, the net consequences of these replacement processes from titanite to fergusonite-(Y) and gadolinite-(Y) is preferential enrichment in HREE, with only a small amount of LREE being retained by altered titanite (3) and synchysite-(Ce).

Combined BSE imaging and EMPA analyses show that alteration of gadolinite-(Y) (Fig. 3l) results in a reduction of total REE, especially HREE. However, the altered zones of gadolinite-(Y) do not contain any detectable F, suggesting that the hydrothermal fluid at this stage was significantly different from those responsible for the early alteration of titanite, rutile, and fergusonite-(Y). It is also interesting to note that the altered zones of gadolinite-(Y) contain higher P_2O_5 and SO_3 contents than their unaltered counterparts but have no detectable F (Fig. 6a), suggesting a fluid enriched PO_4^{3-} and SO_4^{2-} but poor in F^-, different from the F-CO_2-rich fluids replacing titanite, rutile and fergusonite-(Y). Previous studies (Wood, 1990; Lee and Byrne, 1992; Pan et al., 1993; Bern et al., 2017; Ichimura et al., 2020) documented that ground waters commonly contain elevated PO_4^{3-} and SO_4^{2-}, which are capable of forming stable complexes with REE^{3+}. It might be reasonable to infer that the fluid for the alteration of gadolinite-(Y) had a significant component from ground waters.

However, this REE remobilization related to late gadolinite-(Y) alteration resulted in an opposite fractionation between HREE and LREE in the CGBG at Gucheng.

HREE enrichment and mineralization in the Gucheng deposit

Most previous studies of ion-adsorption REE deposits emphasized HREE enrichment during the chemical weathering processes, while several studies suggested that HREE can be accumulated preferentially during the late magmatic stages of granites (Huang et al., 1988; Li et al., 2017a). The latter suggestion is clearly evidenced by the formation of HREE-enriched magmatic titanite 1 and 2 in the CGBG at Gucheng (Fig. 12a). In particular, the HREE-enriched composition of magmatic titanite at Gucheng is distinct from the LREE-enriched characteristics of the host CGBG, thus contributing to the HREE mineralization in this deposit.

More importantly, subsequent hydrothermal alteration of magmatic titanite leads to further HREE enrichments before the chemical weathering process at Gucheng. The magmatic titanite from the CGBG was most likely replaced by a high temperature magmatic-hydrothermal fluid rich in F and CO_3^{2-} (Fig. 12b). The titanite was altered into fergusonite-(Y), rutile, quartz and calcite. During this process, the hydrothermal fluid had leached a large proportion of HREE and LREE (except for La and Ce) out of the magmatic titanite, whilst the La and Ce were retained in the magmatic titanite (Fig. 4c). Therefore, the increased La and Ce in the alteration assemblages were very likely sourced from the magmatic allanite-(Ce) in the CGBG. Indeed, the La (45,374 to

54,942 ppm) and Ce contents (100,441 to 115,022 ppm) of allanite 1 decrease to 33,300 to 38,580 ppm and 71,350 to 84,952 ppm, respectively in allanite 2 (Fig. 7a). Meanwhile, a portion of HREE out of the magmatic titanite was transformed by hydrothermal fluid and then accommodated in the altered zones of the magmatic allanite with HREE increasing from allanite 2 (2,365 to 5,059 ppm; avg. 3,815 ppm) to allanite 1 (4,485 to 8,497 ppm; avg. 6,511 ppm) (Fig. 7a). On the other hand, fergusonite-(Y) also trapped dominant HREE and minor LREE, and significant amounts of REE were scavenged by rutile. Subsequently, another F-rich magmatic-hydrothermal fluid replaced the fergusonite-(Y) and rutile (Fig. 12c), resulting in the further fractionation of LREE and HREE, i.e., HREE decrease and LREE increase in the altered fergusonite-(Y) and the rutile was transformed into HREE-rich gadolinite-(Y) and LREE-dominant synchysite-(Ce). Likewise, gadolinite-(Y) and synchysite-(Ce) are susceptible for chemical weathering (Fig. 12d), and their decomposition could have marked effects on the REE compositions of weathering profiles (Huang et al., 1988; Li et al., 2017a), which is an important mechanism for HREE and LREE mineralization at the Gucheng deposit. Synchysite-(Ce) also appeared to have formed from the release of LREE associated with the alteration of magmatic allanite. However, this process of LREE remobilization and enrichment associated with the alteration of magmatic allanite has minimal effects on HREE. At Gucheng, the magmatic apatite from the CGBG contains some REE but does not show obvious replacement by hydrothermal fluids, limiting the liberation of REE. Moreover, the CGBG apatite has a lower REE content than that of the magmatic titanite and allanite-

(Ce). Apatite has been proven to be more resistant to the weathering process (Li et al., 2019), suggesting that the magmatic apatite of the CGBG might have minimal influence on the formation of the Gucheng deposit.

Above all, complex hydrothermal replacement processes occurring at Gucheng can favorably transform REE-bearing minerals (i.e., titanite and allanite) to forms that are more easily weathered, especially the HREE-enriched minerals, through REE remobilization and re-enrichment. Similar replacement processes involving REE-bearing magmatic minerals (e.g., allanite, apatite, titanite, xenotime and zircon) have also been documented in many other iso-adsorption REE deposits (Huang et al., 1988; Ishihara et al., 2008; Sanematsu and Watanabe, 2016; Bern et al., 2017; Li et al., 2019), granites (Pan et al., 1993), alkaline rocks (Bern et al., 2017), porphyry Cu-Mo deposits (Cao et al., 2015), and iron-oxide copper gold deposits (Xiao et al., 2021). However, metasomatic alteration of magmatic titanite followed by enrichment of HREE as reported in this study is a new observation and may play an important role in HREE mineralization during formation of iso-adsorption REE deposits in South China.

IMPLICATIONS

The fractionation of LREE and HREE during the weathering processes is common in ion-adsorption REE deposits (Li et al., 2017a). An explanation for this fractionation is that LREE ions are preferentially retained on exchange sites in the clay minerals (Bruque et al., 1980), whilst HREE ions are preferentially mobilized

from the upper levels of the weathering profile and enrichened in the lower levels (Bao and Zhao, 2008; Sanematsu et al., 2013; Li et al., 2017a). However, this explanation is focused on the effects of chemical weathering. Our study reveals that REE-bearing magmatic minerals and their alteration products, before chemical weathering, can also contribute to significant fractionation of LREE and HREE towards HREE enrichment for the formation of ion-adsorption HREE deposits. These discoveries are important for understanding the processes behind the genesis of ion-adsorption REE deposits in South China. Moreover, the occurrences of magmatic titanite in granites, especially those with replacement by secondary REE-rich minerals, can be an effective vector in the search for HREE mineralization in South China and elsewhere around the world.

ACKNOWLEDGEMENTS

This study was funded by the Guangdong Major Project of Basic and Applied Basic Research (No. 2019B030302013), the National Natural Science Foundation of China (No. 41725009, 42103058, 41921003, 42173065) and Science and Technology Planning of Guangdong Province, China (2020B1212060055). Staff of the Key Geology Bureau for Nonferrous Metals of Guangdong Province are thanked for supporting the research and for providing access to drill cores and sample collection.

REFERENCES CITED

Aleinikoff, J.N., Wintsch, R.P., Fanning, C.M., and Dorais, M.J. (2002) U-Pb geochronology of zircon and polygenetic titanite from the Glastonbury Complex, Connecticut, USA: an integrated SEM, EMPA, TIMS, and SHRIMP study. Chem. Geol, 188, 125–147.

Bao, Z.W., and Zhao, Z.H. (2003) Geochemistry and tectonic setting of the Fogang aluminous A-type granite, Guangdong Province, China–a preliminary study. Geol. Geochem, 31, 52–61 (in Chinese with English abstract).

Bern, C.R., Yesavage, T., and Foley, N.K. (2017) Ion-adsorption REEs in regolith of the Liberty Hill pluton, South Carolina, USA: An effect of hydrothermal alteration. J. Geochem. Explor, 172, 29–40.

Broska, I., Harlov, D., Tropper, P., and Siman, P. (2007) Formation of magmatic titanite and titanite–ilmenite phase relations during granite alteration in the Tribeč Mountains, Western Carpathians, Slovakia. Lithos, 95, 58–71.

Bruque, S., Mozas, T., and Rodriguez, A. (1980) Factors influencing retention of lanthanide ions by montmorillonite. Clay Miner, 15, 413–420.

Cao, M.J., Qin, K.Z., Li, G.M., Evans, N.J., and Jin, L.Y. (2015) In situ LA-(MC)-ICP-MS trace element and Nd isotopic compositions and genesis of polygenetic titanite from the Baogutu reduced porphyry Cu deposit, Western Junggar, NW China. Ore Geol. Rev, 65, 940–954.

Chakhmouradian, A.R., and Zaitsev, A.N. (2002) Calcite-amphibole-clinopyroxene rock from the Afrikanda complex, Kola Peninsula, Russia: mineralogy and a possible link to carbonatites. III. Silicate minerals. Can. Mineral, 40, 1347–1374.

Chakhmouradian, A.R. (2004) Crystal chemistry and paragenesis of compositionally unique (Al-, Fe-, Nb-, and Zr-rich) titanite from Afrikanda, Russia. Am. Mineral, 89, 1752–1762.

Chi, R., Tian, J., Luo, X., Xu, Z., and He, Z. (2012) The basic research on the weathered crust elution-deposited rare earth ores. Nonferrous Met. Sci. Eng, 3,

1–13 (in Chinese with English abstract).

Feng, Y.Z., Xiao, B., Chu, G.B., Li, S.S., Wang, J., and Wen, Z.Q. (2022) Late Mesozoic magmatism in the Gucheng district: Implications for REE metallogenesis in South China. Ore Geol. Rev, 148, 105034.

Fu, Y., Sun, X.M., Zhou, H.Y., Lin, H., and Yang, T.J. (2016) In-situ LA-ICP-MS U-Pb geochronology and trace elements analysis of polygenetic titanite from the giant Beiya gold-polymetallic deposit in Yunnan Province, Southwest China. Ore Geol. Rev, 77, 43–56.

Gao, X.Y., Zheng, Y.F., Chen, Y.X., and Guo, J.L. (2012) Geochemical and U-Pb age constraints on the occurrence of polygenetic titanites in UHP metagranite in the Dabie orogen. Lithos, 136–139, 93–108.

Hayden, L.A., Watson, E.B., and Wark, D.A. (2008) A thermobarometer for sphene (titanite): Contrib. Mineral. Petrol, 155, 529–540.

Harlov, D., Tropper, P., Seifert, W., Nijland, T., and Forster, H.J. (2006) Formation of Al-rich titanite ($CaTiSiO_4O$-$CaAlSiO_4OH$) reaction rims on ilmenite in metamorphic rocks as a function of fH_2O and fO_2. Lithos, 88, 72–84.

Hu, Z.C., Zhang, W., Liu, Y.S., Gao, S., Li, M., Zong, K.Q., Chen, H.H., and Hu, S.H. (2014) “Wave” signal-smoothing and mercury-removing device for laser ablation quadrupole and multiple collector ICPMS analysis: application to lead isotope analysis. Analytical Chemistry, 87(2), 1152–1157.

Huang, D.H., Wu, C.Y., and Han, J.Z. (1988) REE Geochemistry and Mineralization Characteristics of the Zudong and Guanxi Granites, Jiangxi Province. Acta Geol. Sin, 2(2), 139–157.

Ichimura, K., Sanematsu, K., Kon, Y., Takagi, T., and Murakami, T. (2020) REE redistributions during granite weathering: Implications for Ce anomaly as a proxy for paleoredox states. Am. Mineral, 105(6), 848–859.

Ishihara, S., Renmin, H., Hoshino, M., and Murakami, H. (2008) REE abundance and REE minerals in granitic rocks in the Nanling Range, Jiangxi Province, Southern China, and generation of the REE-rich weathered crust deposits. Resour. Geol, 58, 355–372.

Jamtveit, B. (1991) Oscillatory zonation patterns in hydrothermal grossular-andradite garnet; nonlinear dynamics in regions of immiscibility. Am. Mineral, 76, 1319–1327.

Jowitt, S., Wong, V., Wilson, S., and Gore, O. (2017) Critical metals in the critical zone: controls, resources and future prospectivity of regolith-hosted rare earth elements. Australian Journal of Earth Sciences, 64, 1045–1054.

Lee, H.G., and Byrne, R.H. (1992) Examination of comparative rare earth element complexation behavior using linear free-energy relationships. Geochim. Cosmochim. Acta, 56, 1127–1137.

Li, M.Y.H., Zhao, W.W., and Zhou, M.F. (2017a) Nature of parent rocks, mineralization styles and ore genesis of regolith-hosted REE deposits in South China: An integrated genetic model. Journal of Asian Earth Sciences, 148, 65–95.

Li, X.C., and Zhou, M.F. (2017b) Hydrothermal alteration of monazite-(Ce) and chevkinite-(Ce) from the Sin Quyen Fe-Cu-LREE-Au deposit, northwestern Vietnam. Am. Mineral, 102, 1525–1541.

Li, M.Y.H., Zhou, M.F., and Williams-Jones, A.E. (2019) The Genesis of Regolith-Hosted Heavy Rare Earth Element Deposits: Insights from the World-Class Zudong Deposit in Jiangxi Province, South China. Econ. Geol, 114(3), 541–568.

Li, M.Y.H., and Zhou, M.F. (2020) The role of clay minerals in formation of the regolith-hosted heavy rare earth element deposits. Am. Mineral, 105, 92–108.

Murakami, H., and Ishihara, S. (2008) REE mineralization of weathered crust and clsy sediment on granitic rocks in the Sanyo Belt, SW Japan and the Southern Jiangxi Province, China. Resource Geol, 58, 373–401.

Pan, Y.M., and Fleet, M.E. (1991) Vanadian allanite-(La) and vanadian allanite-(Ce) from the Hemlo gold deposit, Ontario, Canada. Mineral. Mag, 55, 497–507.

Pan, Y.M., Fleet, M.E., and Macrae, N.D. (1993) Late alteration in titanite (CaTiSiO5): Redistribution and remobilization of rare earth elements and implications for U/Pb and Th/Pb geochronology and nuclear waster disposal. Geochim. Cosmochim. Acta, 57, 355–367.

Sanematsu, K., Kon, Y., Imai, A., Watanabe, K., and Watanabe, Y. (2013)

Geochemical and mineralogical characteristics of ion-adsorption type REE mineralization in Phuket, Thailand. Mineral. Deposita, 48, 437–451.

Sanematsu, K., and Watanabe, Y. (2016) Characteristics and genesis of ion-adsorption type deposits. Rev. Econ. Geol, 18, 55–79.

Spandler, C., and Hammerli, J. (2016) MKED1: A new titanite standard for in situ analysis of Sm-Nd isotopes and U-Pb geochronology. Chem. Geol, 425(1), 110–126.

Van Hinsberg, V.J., Migdisov, A.A., and Williams-Jones, A.E. (2010) Reading the mineral record of fluid composition from element partitioning. Geology, 38, 847–850.

Wen, G., Li, J.W., Hofstra, A.H., Koenig, A.E., and Cui, B.Z. (2020) Textures and compositions of clinopyroxene in an Fe skarn with implications for ore-fluid evolution and mineral-fluid REE partitioning. Geochim. Cosmochim. Acta, 290, 104–123.

Wood, S.A. (1990) The aqueous geochemistry of the rare-earth elements and yttrium. 1. Review of available low-temperature data for inorganic complexes and the inorganic REE speciation of natural waters. Chem. Geol, 82, 159–186.

Xiao, B., Pan, Y.M., Song, H., Song, W.L., Zhang, Y., and Chen, H. (2021) Hydrothermal alteration processes of fluorapatite and implications for REE remobilization and mineralization. Contrib. Mineral. Petrol, 176, 87.

Xie, L., Wang, R.C., Chen, J., and Zhu, J.C. (2010) Mineralogical evidence for magmatic and hydrothermal processes in the Qitianling oxidized tin-bearing granite (Hunan, South China): EMP and (MC)-LA-ICPMS investigations of three types of titanite. Chem. Geol, 276, 53–68.

Xu, C., Kynický, J., Smith, M.P., Kopriva, A., Brtnichý, M., Urubek, T., Yang, Y.H., Zhao, Z., He, C., and Song, W.L. (2017) Origin of heavy rare earth mineralization in South China. Nat. Commun, 8, 14598.

Xu, L., Hu, Z.C, Zhang, W., Yang, L., Liu, Y.S., and Gao, S. (2015) In situ Nd isotope analyses in geological materials with signal enhancement and non-linear mass dependent fractionation reduction using laser ablation MC-ICP-MS. J. Anal. At.

Spectrom, 30(1), 232–244.

Yan, S., Zhou, R.J., Niu, H.C., Feng, Y.X., Nguyen, A.D., Zhao, Z.H., Yang, W.B., Dong, Q., and Zhao, J.X. (2020) LA-MC-ICP-MS U-Pb dating of low-U garnets reveals multiple episodes of skarn formation in the volcanic-hosted iron mineralization system, Awulale belt, Central Asia. GSA Bulletin, 132, (5-6), 1031–1045.

Zhang, W., Hu, Z.C., and Liu, Y.S. (2020) Iso-Compass: new freeware software for isotopic data reduction of LA-MC-ICP-MS. J. Anal. At. Spectrom, 35, 1087–1096.

Zhao, W.W., Zhou, M.F., Li, M.Y.H., Zhao, Z., and Gao, J.F. (2017) Genetic types, mineralization styles and geodynamic settings of Mesozoic tungsten deposits in South China. J. Asian Earth Sci, 37, 109–140.

FIGURE CAPTIONS

Figure 1. The distribution of granites and volcanic rocks in south China (after Li et al., 2019). The location of the Gucheng deposit is marked by a blue dot.

Figure 2. Geologic map of the Gucheng ore district showing locations of the ZK03 and ZK06 drill holes.

Figure 3. Photomicrographs showing titanite and its alteration products at Gucheng. (a) A subhedral titanite grain containing a magnetite inclusion in the interstices of quartz and plagioclase; (b) BSE image of (a) showing three texturally and compositionally distinct types of titanite; (c) Magmatic hornblende partially pseudomorphed by an assemblage of titanite, apatite, and magnetite; (d-e) magmatic titanite almost completely peudomorphed by rutile, calcite, quartz, and HREE-rich fergusonite; (f-g) Rutile in a magmatic titanite pseudomorph showing further alteration to gadolinite; (h) Magmatic allanite (1) with an altered rim (2) and synchysite-(Ce) along the rim; (i) Fergusonite grain showing partial dissolution; (j) Rutile partially replaced by gadolinite; (k) Rutile partially replaced by synchysite-(Ce) along the margin; (l) Gadolinite grain showing partial dissolution. Aln-allanite; Ap-apatite; Bt-biotite; Cal-calcite; Chl-chlorite; Fgs-fergusonite; Gad-gadolinite; Hbl-hornblende; Kfsp-K-feldspar; Mag-magnetite; Ms-muscovite; Pl-plagioclase; Qz-quartz; Rt-rutile; Syn-synchysite; Ttn-titanite.

Figure 4. (a) Ranges in the TiO_2, SiO_2, CaO, Al_2O_3, and FeO contents for the three titanite types; (b) Ranges in the Y, Nb, Ta, Zr, and Hf content for the three titanite types; (c) Chondrite-normalized REE patterns of the three titanite types; (d) A BSE image showing the three titanite types; (e-l) Trace element mapping of titanite by LA-ICP-MS for Gd, Tb, Dy, Ho, Er, Tm, Yb, and Lu.

Figure 5. (a) The ranges in the Nb_2O_5, Y_2O_3, SiO_2, CaO, WO_3, ThO_2, UO_2, and F content for the two types of fergusonite; (b) The ranges in the La_2O_3, Ce_2O_3, Pr_2O_3, Nd_2O_3, Sm_2O_3, Dy_2O_3, Ho_2O_3, Er_2O_3, Yb_2O_3, and Lu_2O_3 content for the two types of fergusonite; (c) A BSE image showing two types of fergusonite; (d-k) Trace element mapping of fergusonite by LA-ICP-MS for La, Ce, Nd, Sm, Dy, Ho, Er, and Yb.

Figure 6. (a) The ranges in the TiO_2, SiO_2, Al_2O_3, FeO, CaO, P_2O_5, and Y_2O_3 content for the two types of gadolinite; (b) The ranges in the La_2O_3, Ce_2O_3, Pr_2O_3, Nd_2O_3, Sm_2O_3, Tb_2O_3, Dy_2O_3, Ho_2O_3, Er_2O_3; Yb_2O_3 and Lu_2O_3 content for the two types of gadolinite; (c) A BSE image showing two types of gadolinite; (d-h) Trace element mapping of gadolinite by LA-ICP-MS for Ce, Nd, Sm, Dy, and Er.

Figure 7. Chondrite-normalized plots of the REE compositions for allanite (a) and apatite (b) from the CGBG at Gucheng.

Figure 8. LA-ICP-MS U-Pb Tera-Wasserburg concordia diagram for magmatic

titanite.

Figure 9. Diagram showing range of $(^{143}Nd/^{144}Nd)_i$ values for titanite 1 and 2; (b) Histograms showing the variations in εNd(t) for titanite (this study) and CGBG whole rock data.

Figure 10. Plots of LREE (ppm) vs. Ca (apfu) (a), HREE (ppm) vs. Ca (apfu) (b), Ti (apfu) vs. (Al + Fe) (apfu) (c), and Nb + Zr (ppm) vs. (Ti) (apfu) (d) of the three types of titanite at Gucheng CGBG.

Figure 11. Chondrite normalized plots of REE from the titanites 1 and 2 and REE in fergusonite (1/16 and 1/81) and gadolinite (1/18 and 1/90) from the Gucheng CGBG.

Figure 12. Sketches illustrating the various stages of titanite alteration at the Gucheng deposit during two hydrothermal alteration events and during chemical weathering.

TABLE 1. EPMA major and minor elements in fergusonite-(Y) from the Gucheng CGBG (wt%)

	Fgs1	Fgs1	Fgs1	Fgs2	Fgs2	Fgs2	Fgs2
WO_3	9.2	8.8	8.8	0.2	0.9	0.4	0.1
Nb_2O_5	34.6	33.9	32.8	40.7	36.8	38.9	38.6
Ta_2O_5	5.0	6.0	6.0	4.4	3.4	5.1	4.9
SiO_2	0	0	0	7.5	5.6	10.3	9.8
TiO_2	2.0	2.8	2.6	2.4	2.0	1.7	1.9
ThO_2	0.1	0.1	0	2.4	3.2	1.9	2.9
UO_2	0.7	0.5	0.5	3.4	4.6	5.5	5.0
Al_2O_3	0	0	0	0.4	0.1	0.8	0.6
Y_2O_3	30.1	30.4	30.8	6.4	14.2	3.9	6.4
La_2O_3	0.1	0	0	1.2	1.2	1.7	1.5
Ce_2O_3	0	0	0	4.7	3.7	4.1	4.6
Pr_2O_3	0	0	0	0.5	0.4	0.4	0.6
Nd_2O_3	0.2	0.1	0.1	3.8	2.1	2.1	2.9
Sm_2O_3	0.7	1.0	1.6	3.9	2.5	2.1	3.0
Eu_2O_3	0	0	0	0	0	0	0
Gd_2O_3	0.7	0.8	0.8	0.9	0.8	0.6	0.7
Tb_2O_3	0.3	0.4	0.4	0.3	0.4	0	0.2
Dy_2O_3	3.7	4.4	5.0	2.2	2.6	1.1	1.6
Ho_2O_3	0.8	1.3	1.3	0.6	0.8	0.3	0.5
Er_2O_3	4.0	3.9	4.3	1.2	2.1	0.8	1.0
Tm_2O_3	0.2	0	0	0.2	0.2	0.1	0.1
Yb_2O_3	4.5	4.1	4.5	1.2	2.4	0.8	1.1
Lu_2O_3	0.9	1.2	1.0	0.2	0.7	0.2	0.3
CaO	1.1	0.5	0.3	5.6	3.1	6.8	5.9
FeO	0	0.1	0	0.7	0.4	0.8	0.7
F	0	0	0	2.0	2.3	2.9	2.5
Total	99.1	100.5	101.0	96.2	95.7	92.4	96.4

Notes: Fgs = fergusonite-(Y).

TABLE 2. EPMA major and minor elements in rutile from the Gucheng CGBG (wt%)

	WO_3	Nb_2O_5	Ta_2O_5	SiO_2	TiO_2	SnO_2	Al_2O_3	CaO	FeO	Total
Rt1	1.0	0.2	0.1	1.6	92.3	0	0.5	0.5	1.8	98.1
Rt1	2.8	0.3	0.1	0.2	93.4	0	0.2	0.1	2.8	100.0
Rt1	1.7	0.3	0.1	0.1	95.9	0.1	0.1	0.1	2.0	100.5
Rt1	4.5	1.7	0.3	0.1	87.2	0.6	0.2	0.1	4.0	98.9
Rt1	1.4	2.6	0.6	0.0	92.4	0.8	0.0	0	2.4	100.2
Rt1	2.4	0.2	0.1	0.4	94.0	0	0.2	0.2	2.1	99.7
Rt1	1.3	0.1	0.1	1.9	91.0	0	0.7	0.6	2.0	97.7
Rt1	3.6	2.7	1.1	0.0	88.5	0.7	0.1	0	3.7	100.4
Rt2	0.2	2.4	1.1	0.2	95.3	0.1	0.1	0.1	0.7	100.2
Rt2	0.6	0.9	0.5	0.8	95.0	0.1	0.1	0.1	1.2	99.3
Rt2	0.2	2.2	0.1	0.6	96.4	0.1	0	0.1	0.8	100.5
Rt2	0.1	0.5	0.2	2.1	96.3	0	0	0.2	0.7	100.1
Rt2	0.6	1.2	0.4	0.4	95.9	0.2	0	0.1	1.5	100.3
Rt2	0.4	0.9	0.4	0.5	97.2	0	0.1	0.1	1.1	100.6
Rt2	0.3	1.2	0.2	1.4	95.8	0.2	0.1	0	1.5	100.7
Rt2	0.4	1.0	0.1	1.2	96.1	0.1	0	0.1	1.2	100.3
Rt2	0	1.2	0	0.4	93.7	1.4	0.1	0.1	1.3	98.4
Rt2	0	1.9	0	1.5	95.0	0.2	0.1	0.1	1.0	99.9

Notes: Rt = rutile.

TABLE 3. EPMA major and minor elements in gadolinite-(Y) from the Gucheng CGBG (wt%)

	Gd1	Gd1	Gd1	Gd1	Gd1	Gd1	Gd2	Gd2	Gd2	Gd2	Gd2
SO_3	0	0	0	0	0	0	0.02	0.03	0.04	0.04	0.03
P_2O_5	0	0	0	0	0	0	0.05	0.1	0.04	0.05	0.03
Nb_2O_5	0	0	0	0	0	0	0	0	0	0	0
SiO_2	25.0	25.1	25.8	26.2	25.6	26.0	28.6	29.7	28.7	28.7	28.8
TiO_2	0.8	0.8	0.5	0.5	0.9	1.1	0.2	0.4	0.5	0.4	0.5
ThO_2	0.2	0.1	0.2	0.1	0.4	0.2	0.5	0.5	0.2	0.3	0.4
UO_2	0	0.1	0.1	0	0.1	0.1	0	0	0	0	0
Al_2O_3	0	0	0	0	0	0	0.6	1.1	0.7	0.6	0.7
Y_2O_3	29.9	30.1	29.6	29.2	30.0	29.1	26.6	25.4	25.7	26.3	26.0
La_2O_3	0	0.1	0.0	0.1	0	0.1	0.4	0.4	0.4	0.4	0.4
Ce_2O_3	0	0	0.2	0	0	0	2.5	2.3	2.3	2.1	2.0
Pr_2O_3	0	0	0.1	0	0	0	0.4	0.4	0.3	0.3	0.3
Nd_2O_3	0.4	0.2	1.0	0.4	0.6	0.2	3.7	3.6	3.7	4.0	3.4
Sm_2O_3	2.7	1.5	4.7	1.8	2.8	1.0	5.9	5.7	5.5	6.4	5.5
Eu_2O_3	0	0	0	0	0	0	0	0	0	0	0
Gd_2O_3	1.8	1.3	2.0	1.3	1.8	1.1	1.6	1.6	1.4	1.3	1.4
Tb_2O_3	0.3	0.2	0.4	0.4	0.5	0.3	0.3	0.3	0.3	0.1	0.2
Dy_2O_3	5.9	5.1	5.8	5.2	5.3	5.2	4.1	4.0	3.3	4.2	4.3
Ho_2O_3	1.9	1.4	2.0	1.5	2.0	1.6	1.2	1.4	1.6	1.5	1.6
Er_2O_3	3.6	3.4	3.5	3.7	3.7	3.9	1.9	1.8	1.8	1.5	1.9
Tm_2O_3	0.1	0.1	0	0.2	0.1	0	0.1	0	0	0.1	0.1
Yb_2O_3	3.3	3.8	2.9	3.6	2.9	4.2	0.7	0.8	0.6	0.7	0.8
Lu_2O_3	1.2	1.1	1.1	1.1	1.4	1.0	0.7	0.6	0.4	0.3	0.6
CaO	2.0	2.7	2.2	3.6	1.9	2.9	4.5	4.3	4.4	4.6	4.2
FeO	7.7	8.4	6.8	6.7	7.4	9.1	2.6	2.9	3.1	3.1	3.5
Total	87.1	85.6	89.1	85.7	87.4	87.4	87.3	87.5	85.3	87.1	86.6

Notes: Gd = gadolinite-(Y).

TABLE 4. LA-ICP-MS REE elements in allanite and apatite from the Gucheng CGBG (ppm)

	La	Ce	Pr	Nd	Sm	Eu	Gd	Tb	Dy	Ho	Er	Tm	Yb	Lu	REE	LREE	HREE	LR/HR	$(La/Yb)_N$
Aln1	45707	100441	10438	34334	4797	28.3	2255	221	863	123	254	28.2	168	21.0	199678	195744	3934	50	184
Aln1	54942	102574	9350	27716	3030	57.5	1340	127	499	74.5	163	19.7	125	16.4	200035	197670	2365	84	296
Aln1	53801	103544	9660	29169	3398	45.2	1506	139	524	75.7	159	18.0	110	14.1	202164	199618	2546	78	329
Aln1	45374	109625	11432	34547	5046	15.6	2219	242	1006	157	386	55.9	433	65.6	210604	206039	4565	45	71
Aln1	47256	115022	11736	33149	4413	12.8	1714	190	809	128	339	56.6	482	74.3	215381	211588	3793	56	66
Aln1	46648	110322	11632	35911	5119	14.6	2235	232	934	138	320	42.4	298	41.2	213888	209647	4241	49	106
Aln1	45854	102319	10643	34968	4895	24.6	2281	227	885	127	265	29.7	182	22.5	202721	198703	4018	49	170
Aln1	45599	105327	11331	38409	5913	15.9	2857	287	1121	161	337	38.1	228	28.7	211654	206595	5059	41	135
Aln2	37232	81677	8879	28863	4242	25.2	2034	232	1047	178	473	73.2	572	81.9	165609	160917	4692	34	44
Aln2	33300	80511	9152	31422	5250	21.9	2818	362	1856	345	1013	171	1394	198	167813	159657	8156	20	16
Aln2	35288	84952	9101	30398	5013	16.2	2685	358	1927	376	1118	176	1336	190	172935	164769	8165	20	18
Aln2	34123	79573	8886	29728	4864	19.8	2685	362	1945	376	1122	194	1586	227	165691	157194	8497	19	15
Aln2	34526	72428	7775	24855	3652	25.1	1796	216	1057	186	518	85.6	703	101	147924	143261	4663	31	33
Aln2	34261	71350	7592	24255	3456	24.8	1719	210	1006	180	501	82.9	687	99.1	145424	140939	4485	31	34
Aln2	38580	83779	8485	27025	3795	33.4	1959	250	1316	256	754	120	901	127	167380	161697	5682	28	29
Aln2	35563	84715	9132	29891	4908	29.3	2658	354	1856	359	1046	158	1158	159	171984	164237	7747	21	21
Ap	1415	3724	480	1969	389	20.4	350	48.6	271	54.9	141	17.9	106	14.4	9001	7997	1003	8	9
Ap	518	1699	242	1073	273	11.2	285	41.5	249	51.6	144	19.4	120	19.8	4746	3816	930	4	3
Ap	940	2691	363	1533	331	13.2	308	43.0	243	48.0	119	15.3	87.6	11.6	6747	5871	876	7	7
Ap	1604	4048	528	2170	424	20.4	382	51.0	280	53.6	129	15.3	84.8	10.7	9800	8794	1006	9	13
Ap	780	2619	369	1651	398	15.9	410	60.4	359	73.9	196	27.4	170	25.5	7156	5833	1323	4	3
Ap	1451	3676	458	1791	324	16.2	294	38.8	217	41.8	107	13.2	77.3	10.4	8515	7715	799	10	13

Notes: Aln = allanite; Ap = apatite.

TABLE 5. Nd isotopic compositions of titanite of the CGBG in the Gucheng deposit

	$(^{143}Nd/^{144}Nd)^{a}$	Sm (ppm)	Nd (ppm)	$(^{143}Nd/^{144}Nd)_i^{b}$	$\varepsilon Nd(t)^{c}$	T_{2DM}^{d}
Ttn1	0.512377	2738	3441	0.512062	-8.7	1610
Ttn1	0.512360	2710	3676	0.512069	-8.6	1599
Ttn1	0.512400	2636	3145	0.512069	-8.6	1599
Ttn1	0.512351	2730	3793	0.512066	-8.6	1603
Ttn1	0.512404	2744	3389	0.512084	-8.3	1575
Ttn1	0.512394	2555	3328	0.512091	-8.2	1565
Ttn1	0.512391	2495	3294	0.512091	-8.2	1563
Ttn1	0.512378	2784	3978	0.512101	-8.0	1548
Ttn1	0.512382	2614	3689	0.512102	-7.9	1547
Ttn2	0.512379	2689	3705	0.512092	-8.1	1562
Ttn2	0.512396	2601	3562	0.512107	-7.8	1538
Ttn2	0.512405	2941	3889	0.512106	-7.9	1540
Ttn2	0.512348	2622	3698	0.512068	-8.6	1601
Ttn2	0.512377	2459	3373	0.512088	-8.2	1568

Notes: Ttn = titanite.

a Measured $^{143}Nd/^{144}Nd$-ratios.

b Initial $^{143}Nd/^{144}Nd$-ratios.

c $\varepsilon Nd(t) = [(^{143}Nd/^{144}Nd)_i/(^{143}Nd/^{144}Nd)_{CHUR}-1] \times 10000$

d Two-stage Nd model ages.

Figure 1

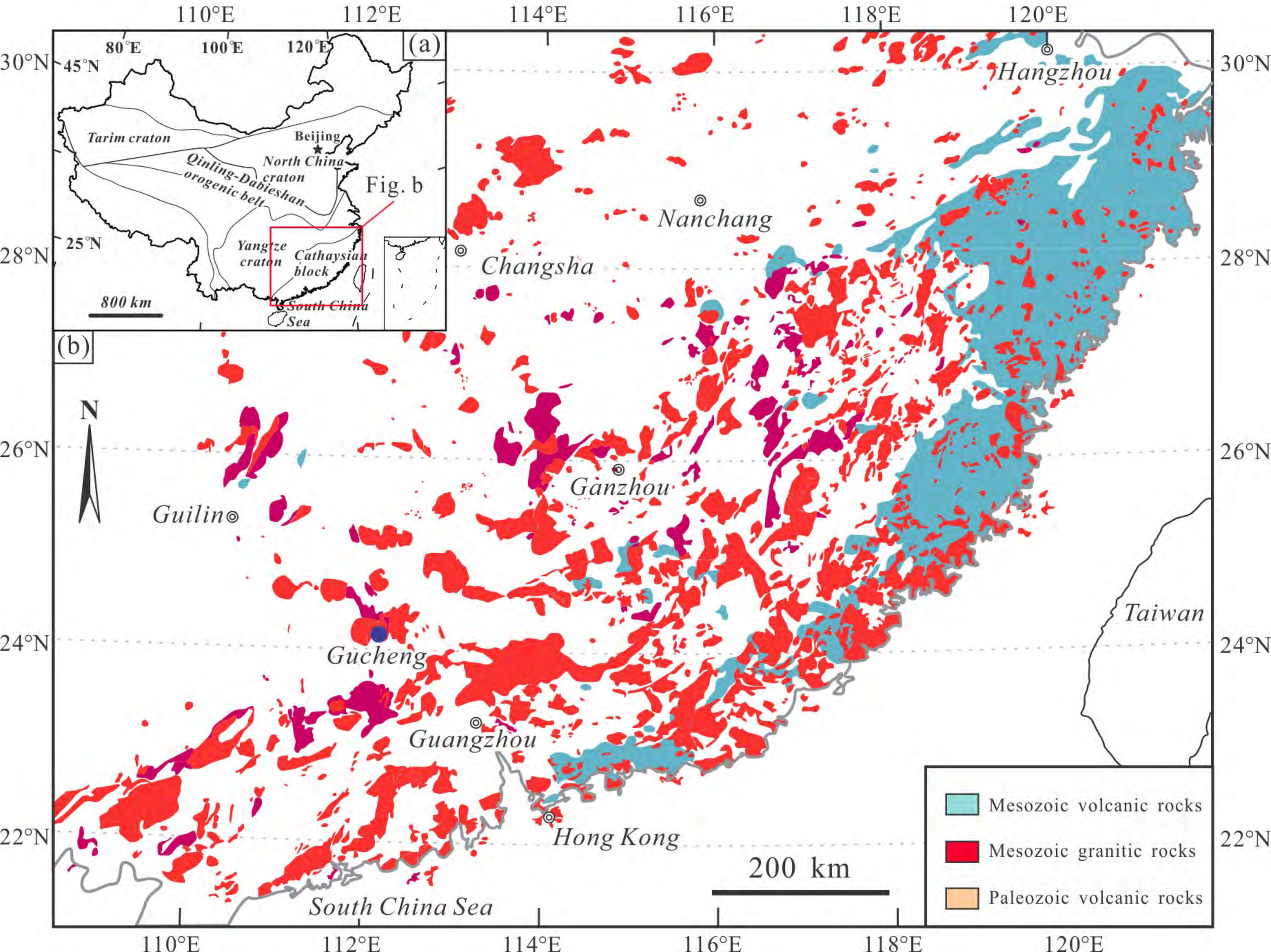
(a)
80°E
100°E
120°E
45°N
25°N
Tarim craton
Beijing
North China craton
Qinling-Dabieshan orogenic belt
Fig. b
Yangtze craton
Cathaysian block
800 km
South China Sea
(b)
110°E
112°E
114°E
116°E
118°E
120°E
30°N
28°N
26°N
24°N
22°N
N
Hangzhou
Nanchang
Changsha
Ganzhou
Guilin
Taiwan
Gucheng
Guangzhou
Hong Kong
200 km
South China Sea
Mesozoic volcanic rocks
Mesozoic granitic rocks
Paleozoic volcanic rocks

Figure 2

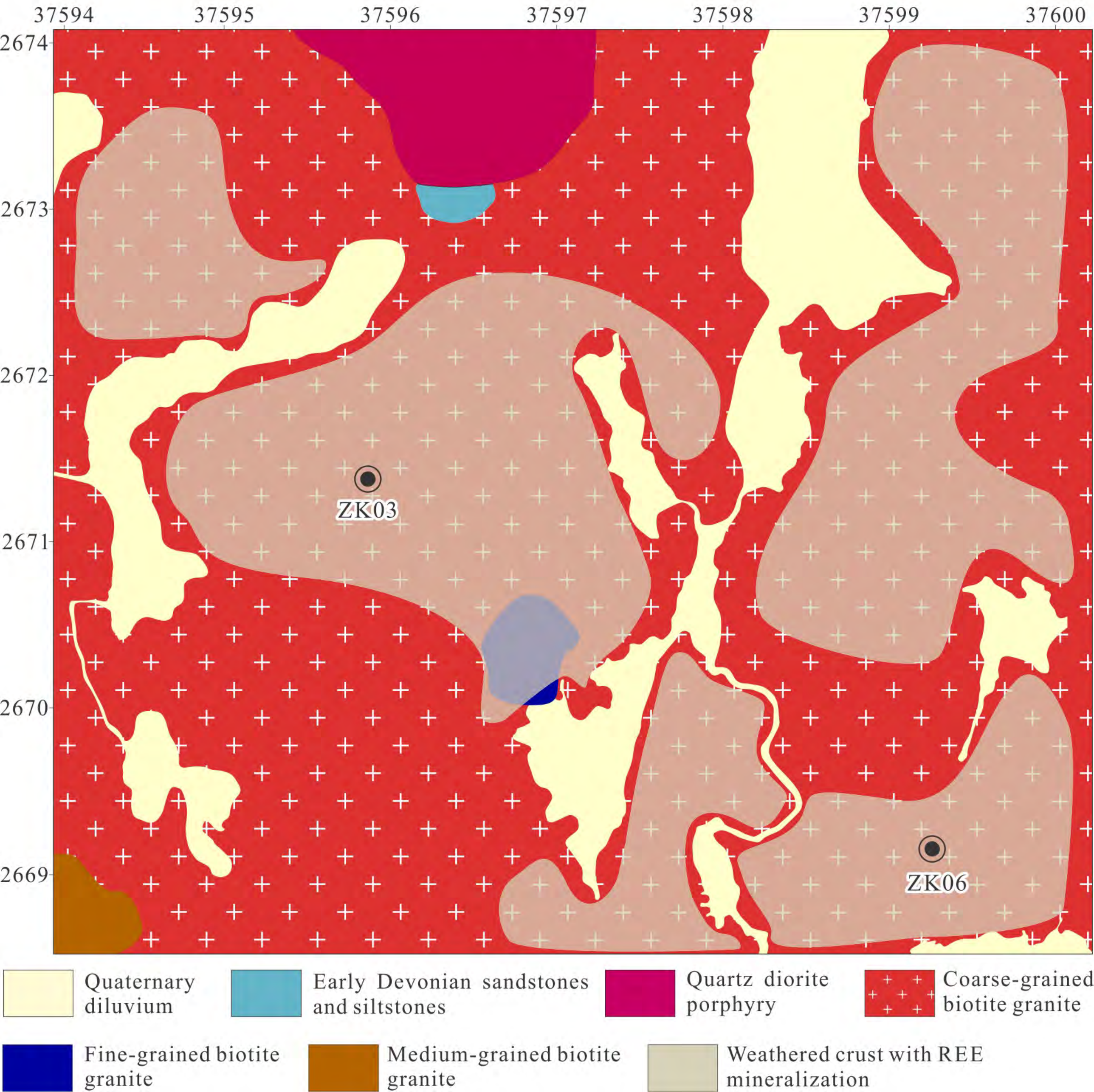
37594
37595
37596
37597
37598
37599
37600
2674
2673
2672
2671
2670
2669
ZK03
ZK06
Quaternary diluvium
Early Devonian sandstones and siltstones
Quartz diorite porphyry
Coarse-grained biotite granite
Fine-grained biotite granite
Medium-grained biotite granite
Weathered crust with REE mineralization

Figure 3

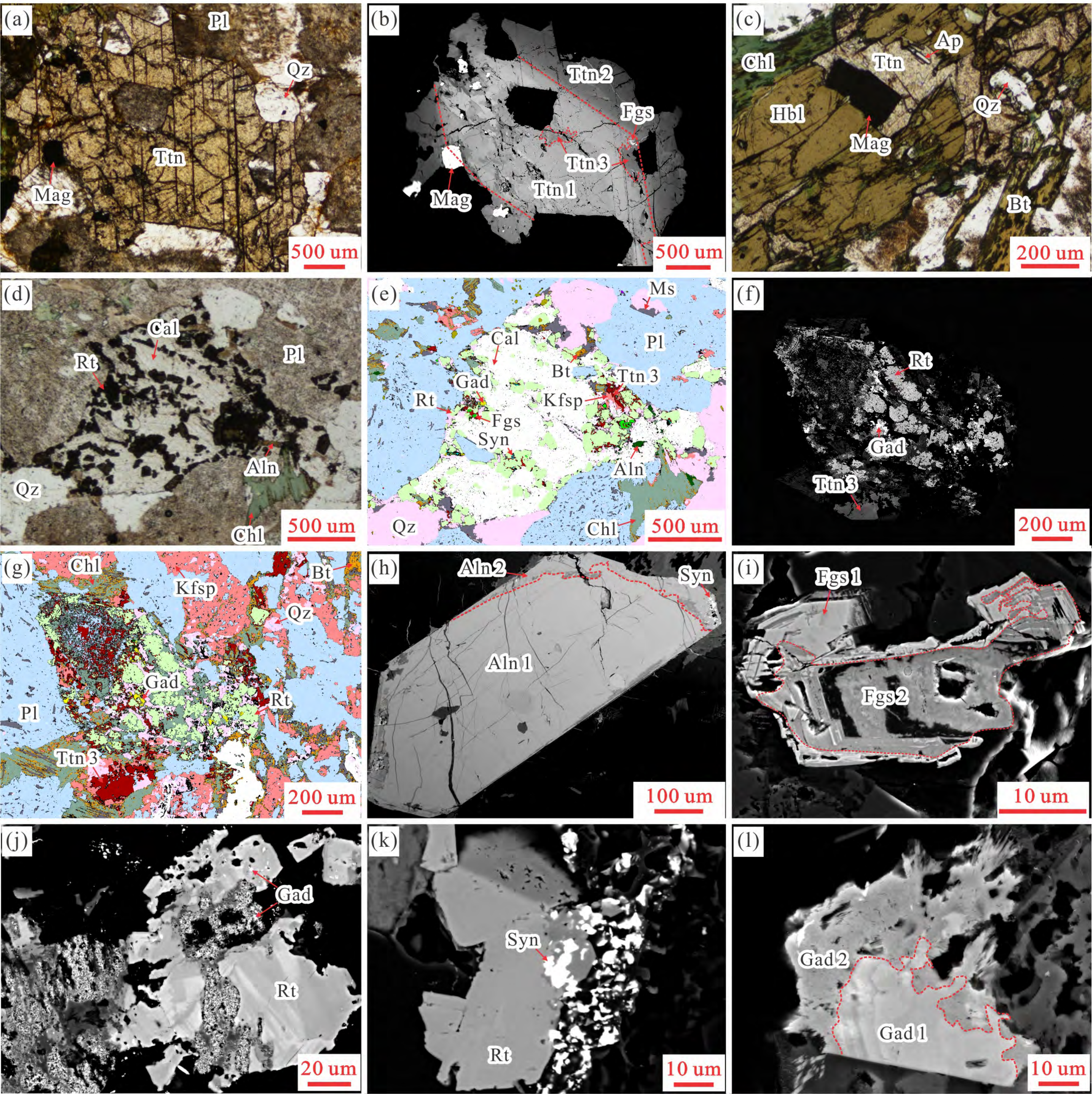
(a)
Pl
Qz
Ttn
Mag
500 um
(b)
Ttn 2
Fgs
Ttn 3
Ttn 1
Mag
500 um
(c)
Ap
Chl
Ttn
Qz
Hbl
Mag
Bt
200 um
(d)
Cal
Rt
Pl
Aln
Qz
Chl
500 um
(e)
Ms
Cal
Pl
Bt
Ttn 3
Gad
Rt
Kfsp
Fgs
Syn
Aln
Qz
Chl
500 um
(f)
Rt
Gad
Ttn 3
200 um
(g)
Chl
Bt
Kfsp
Qz
Gad
Rt
Pl
Ttn 3
200 um
(h)
Aln 2
Syn
Aln 1
100 um
(i)
Fgs 1
Fgs 2
10 um
(j)
Gad
Rt
20 um
(k)
Syn
Rt
10 um
(l)
Gad 2
Gad 1
10 um

Figure 4

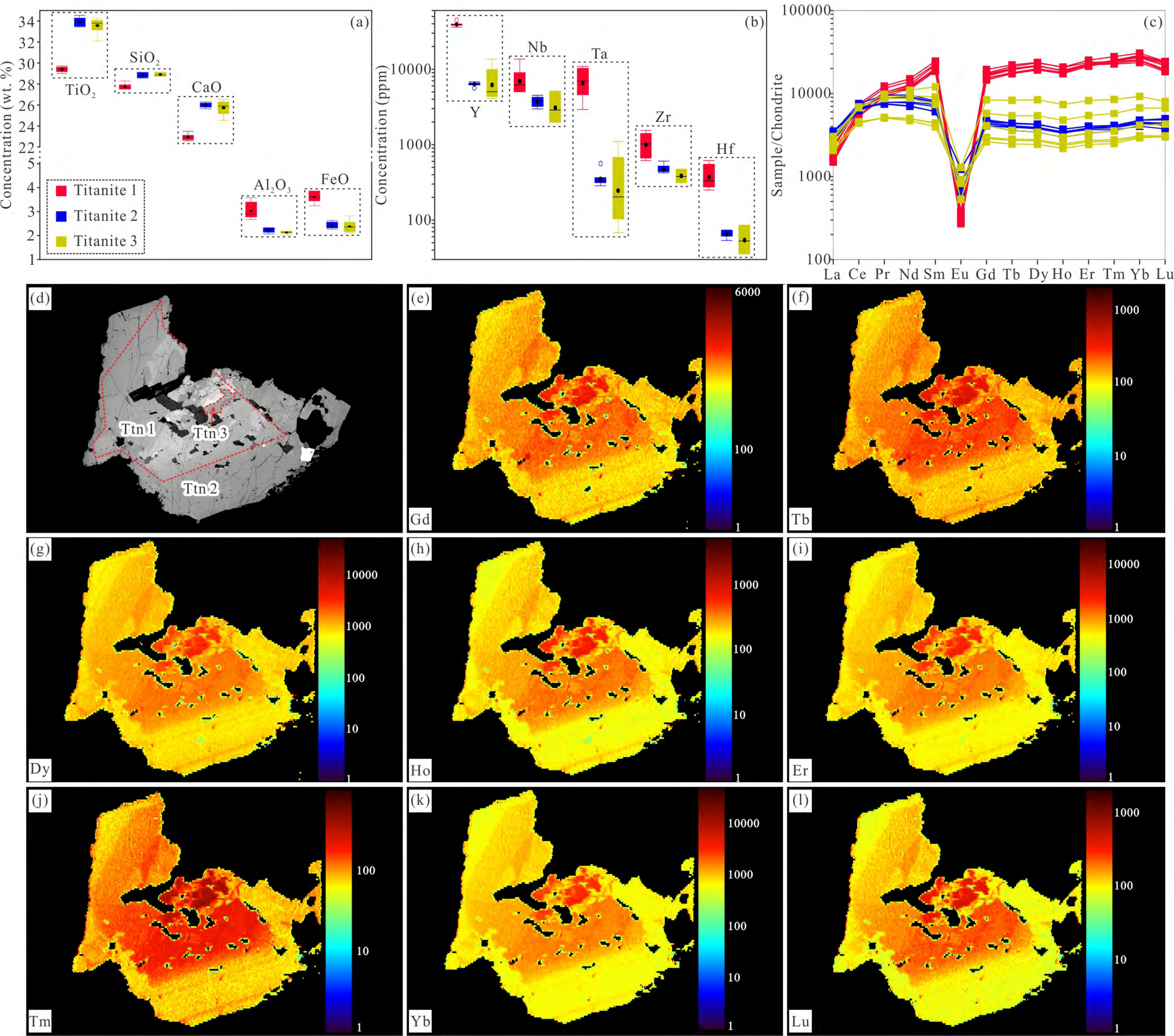
(a)
Concentration (wt. %)
TiO2
SiO2
CaO
Al2O3
FeO
Titanite 1
Titanite 2
Titanite 3
(b)
Concentration (ppm)
Y
Nb
Ta
Zr
Hf
(c)
Sample/Chondrite
La Ce Pr Nd Sm Eu Gd Tb Dy Ho Er Tm Yb Lu
(d)
Ttn 1
Ttn 2
Ttn 3
(e) Gd
(f) Tb
(g) Dy
(h) Ho
(i) Er
(j) Tm
(k) Yb
(l) Lu

Figure 5

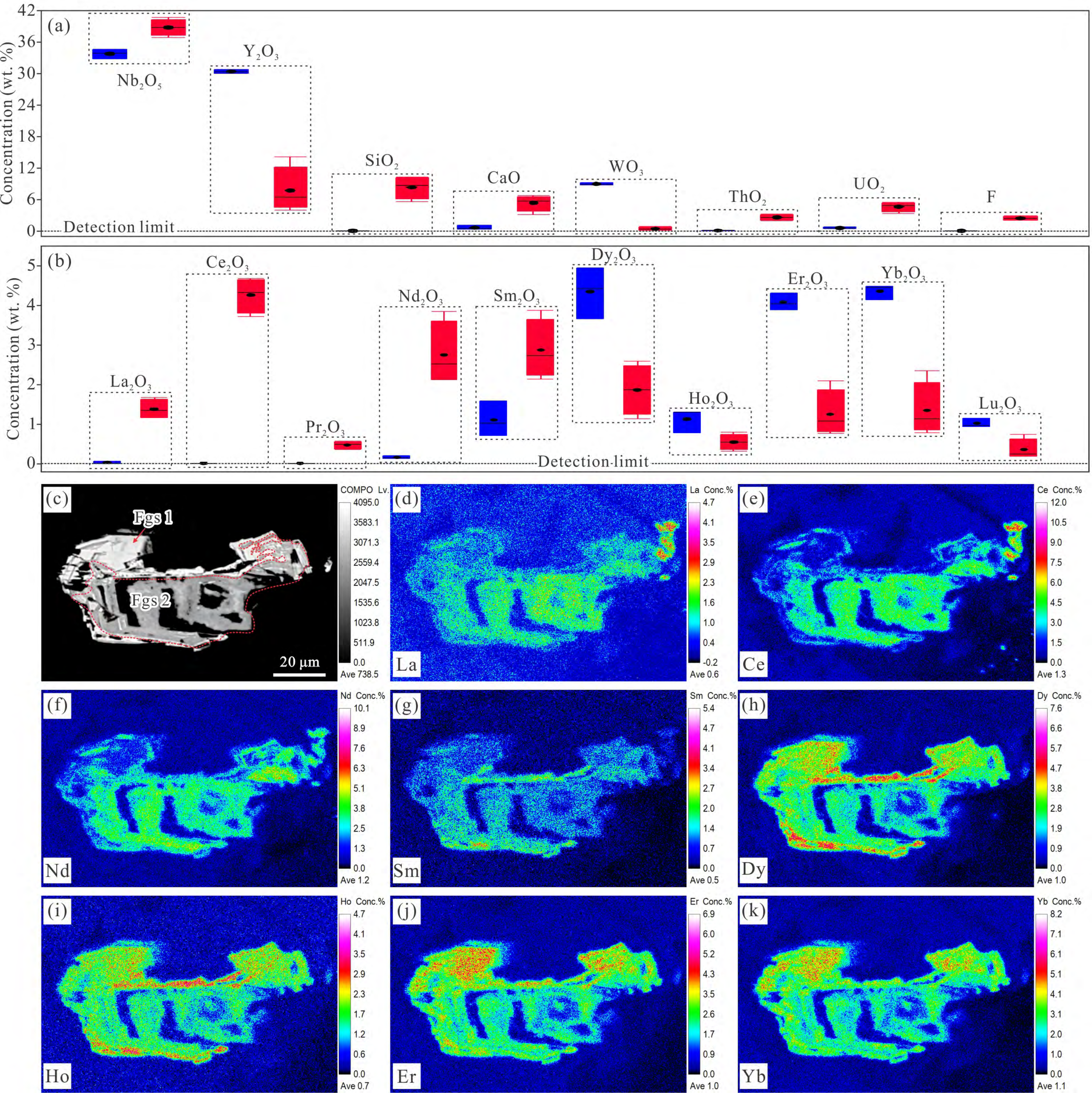
(a)
Concentration (wt. %)
42
36
30
24
18
12
6
0
Nb2O5
Y2O3
SiO2
CaO
WO3
ThO2
UO2
F
Detection limit
(b)
Concentration (wt. %)
5
4
3
2
1
0
La2O3
Ce2O3
Pr2O3
Nd2O3
Sm2O3
Dy2O3
Ho2O3
Er2O3
Yb2O3
Lu2O3
Detection limit
(c)
Fgs 1
Fgs 2
20 μm
COMPO Lv.
4095.0
3583.1
3071.3
2559.4
2047.5
1535.6
1023.8
511.9
0.0
Ave 738.5
(d)
La
La Conc.%
4.7
4.1
3.5
2.9
2.3
1.6
1.0
0.4
-0.2
Ave 0.6
(e)
Ce
Ce Conc.%
12.0
10.5
9.0
7.5
6.0
4.5
3.0
1.5
0.0
Ave 1.3
(f)
Nd
Nd Conc.%
10.1
8.9
7.6
6.3
5.1
3.8
2.5
1.3
0.0
Ave 1.2
(g)
Sm
Sm Conc.%
5.4
4.7
4.1
3.4
2.7
2.0
1.4
0.7
0.0
Ave 0.5
(h)
Dy
Dy Conc.%
7.6
6.6
5.7
4.7
3.8
2.8
1.9
0.9
0.0
Ave 1.0
(i)
Ho
Ho Conc.%
4.7
4.1
3.5
2.9
2.3
1.7
1.2
0.6
0.0
Ave 0.7
(j)
Er
Er Conc.%
6.9
6.0
5.2
4.3
3.5
2.6
1.7
0.9
0.0
Ave 1.0
(k)
Yb
Yb Conc.%
8.2
7.1
6.1
5.1
4.1
3.1
2.0
1.0
0.0
Ave 1.1

Figure 6

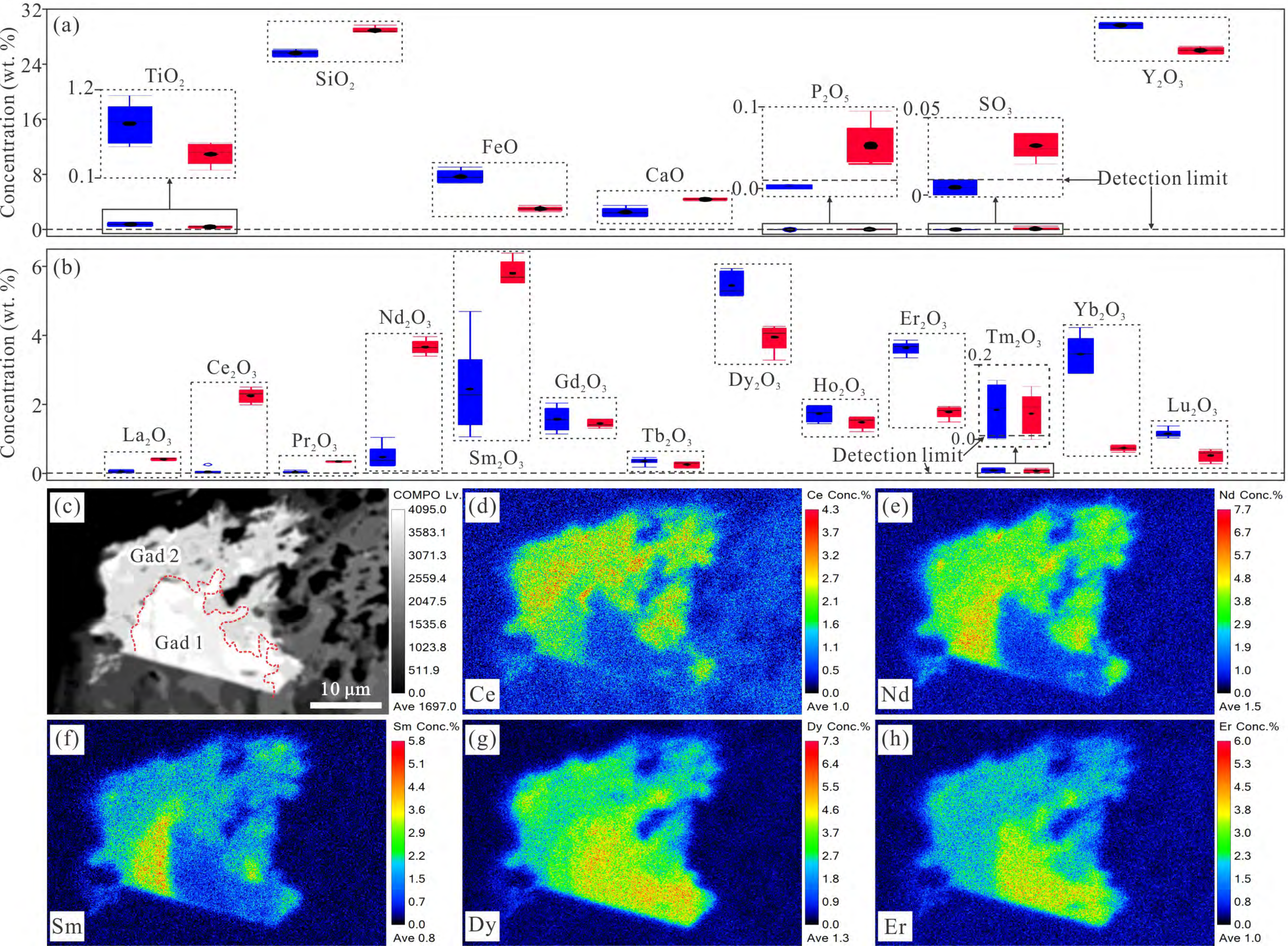
(a)
Concentration (wt. %)
32
24
16
8
0
TiO2
1.2
0.1
SiO2
FeO
CaO
P2O5
0.1
0.0
0.05
SO3
0
Y2O3
Detection limit
(b)
Concentration (wt. %)
6
4
2
0
La2O3
Ce2O3
Pr2O3
Nd2O3
Sm2O3
Gd2O3
Tb2O3
Dy2O3
Ho2O3
Er2O3
Tm2O3
0.2
0.0
Yb2O3
Lu2O3
Detection limit
(c)
Gad 2
Gad 1
10 μm
COMPO Lv.
4095.0
3583.1
3071.3
2559.4
2047.5
1535.6
1023.8
511.9
0.0
Ave 1697.0
(d)
Ce
Ce Conc.%
4.3
3.7
3.2
2.7
2.1
1.6
1.1
0.5
0.0
Ave 1.0
(e)
Nd
Nd Conc.%
7.7
6.7
5.7
4.8
3.8
2.9
1.9
1.0
0.0
Ave 1.5
(f)
Sm
Sm Conc.%
5.8
5.1
4.4
3.6
2.9
2.2
1.5
0.7
0.0
Ave 0.8
(g)
Dy
Dy Conc.%
7.3
6.4
5.5
4.6
3.7
2.7
1.8
0.9
0.0
Ave 1.3
(h)
Er
Er Conc.%
6.0
5.3
4.5
3.8
3.0
2.3
1.5
0.8
0.0
Ave 1.0

Figure 7

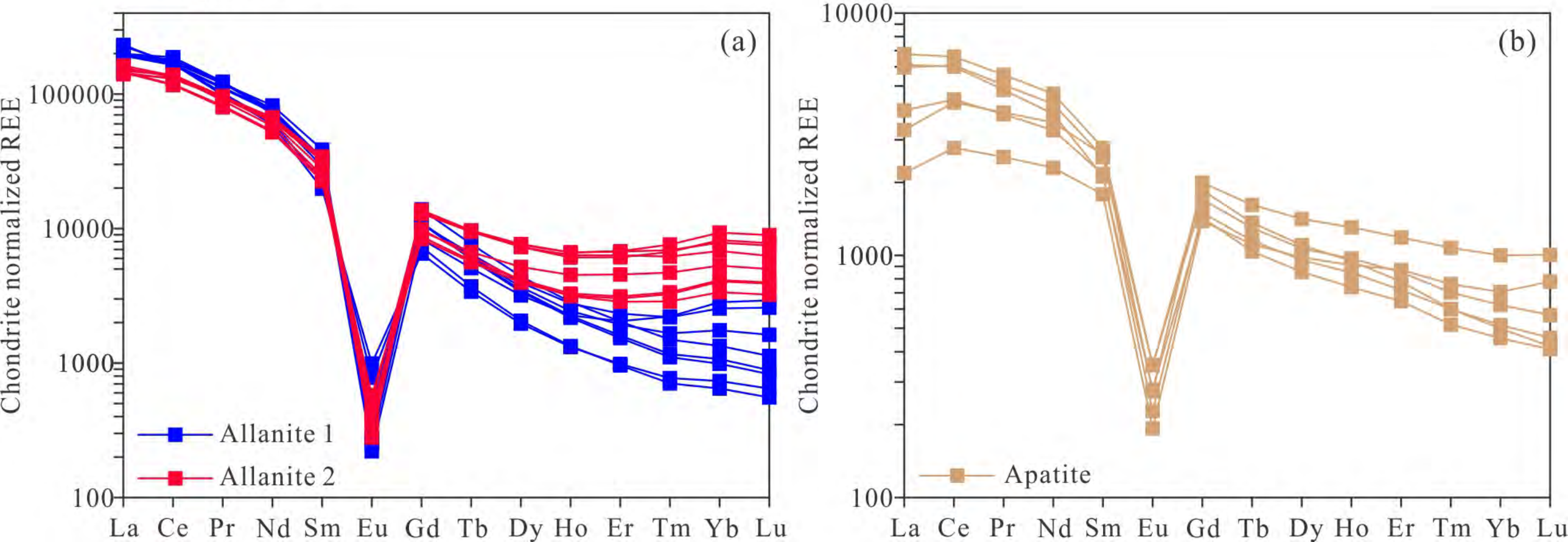
(a)
Chondrite normalized REE
100000
10000
1000
100
Allanite 1
Allanite 2
La Ce Pr Nd Sm Eu Gd Tb Dy Ho Er Tm Yb Lu
(b)
Chondrite normalized REE
10000
1000
100
Apatite
La Ce Pr Nd Sm Eu Gd Tb Dy Ho Er Tm Yb Lu

Figure 8

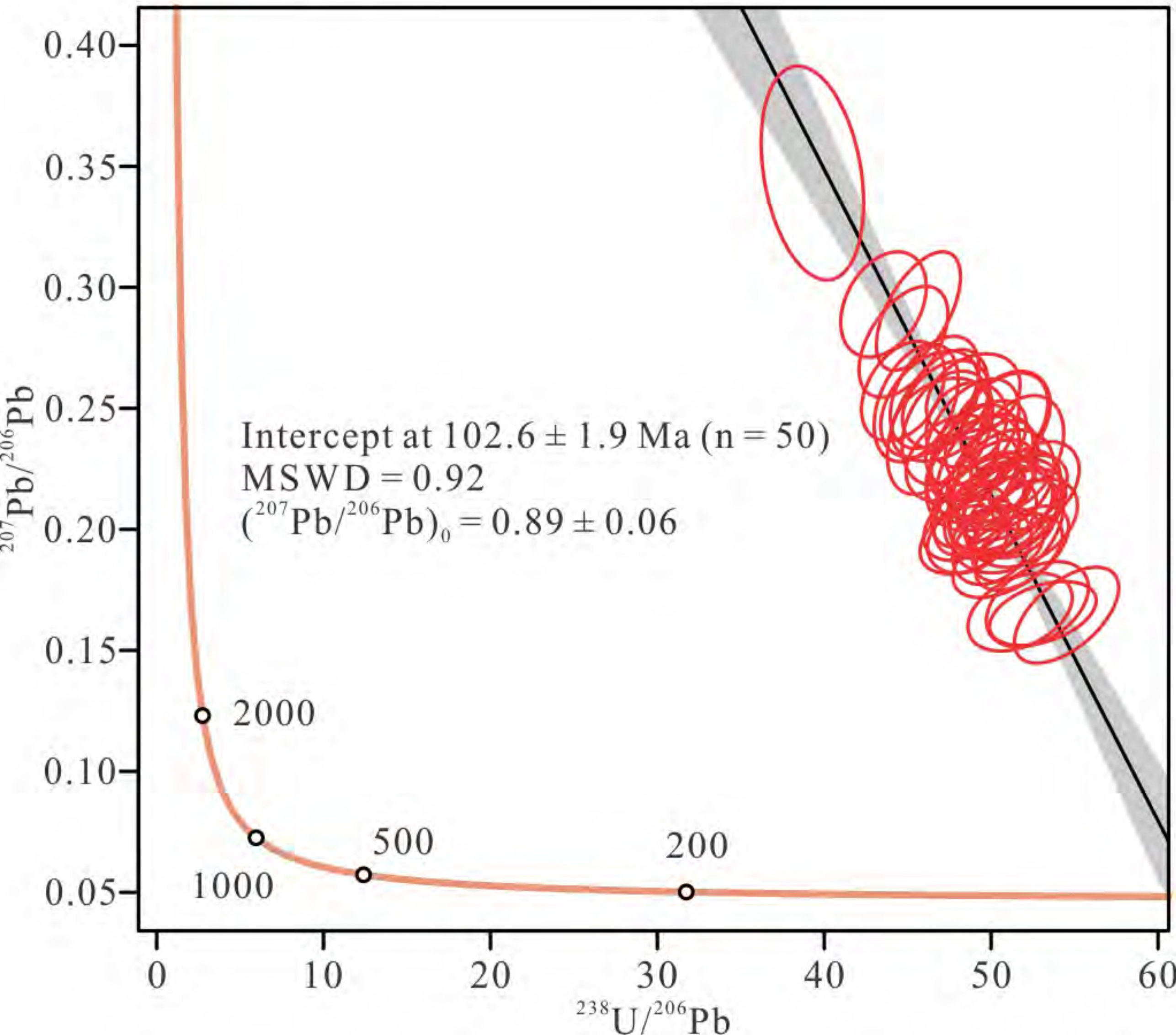
0.40
0.35
0.30
0.25
0.20
0.15
0.10
0.05
$^{207}Pb/^{206}Pb$
Intercept at 102.6 ± 1.9 Ma (n = 50)
MSWD = 0.92
$(^{207}Pb/^{206}Pb)_0 = 0.89 \pm 0.06$
2000
1000
500
200
0
10
20
30
40
50
60
$^{238}U/^{206}Pb$

Figure 9

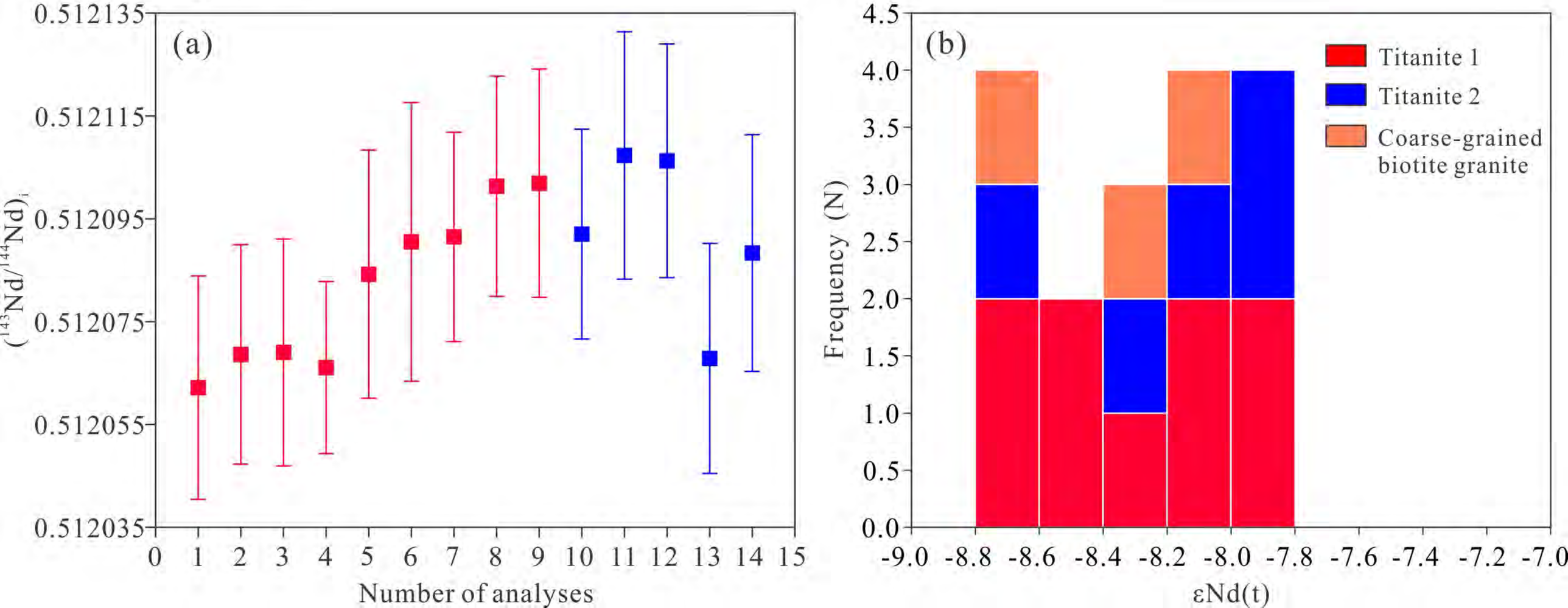
(a)
0.512135
0.512115
0.512095
0.512075
0.512055
0.512035
$(^{143}Nd/^{144}Nd)_i$
0 1 2 3 4 5 6 7 8 9 10 11 12 13 14 15
Number of analyses
(b)
Titanite 1
Titanite 2
Coarse-grained biotite granite
Frequency (N)
0.0 0.5 1.0 1.5 2.0 2.5 3.0 3.5 4.0 4.5
-9.0 -8.8 -8.6 -8.4 -8.2 -8.0 -7.8 -7.6 -7.4 -7.2 -7.0
εNd(t)

Figure 10

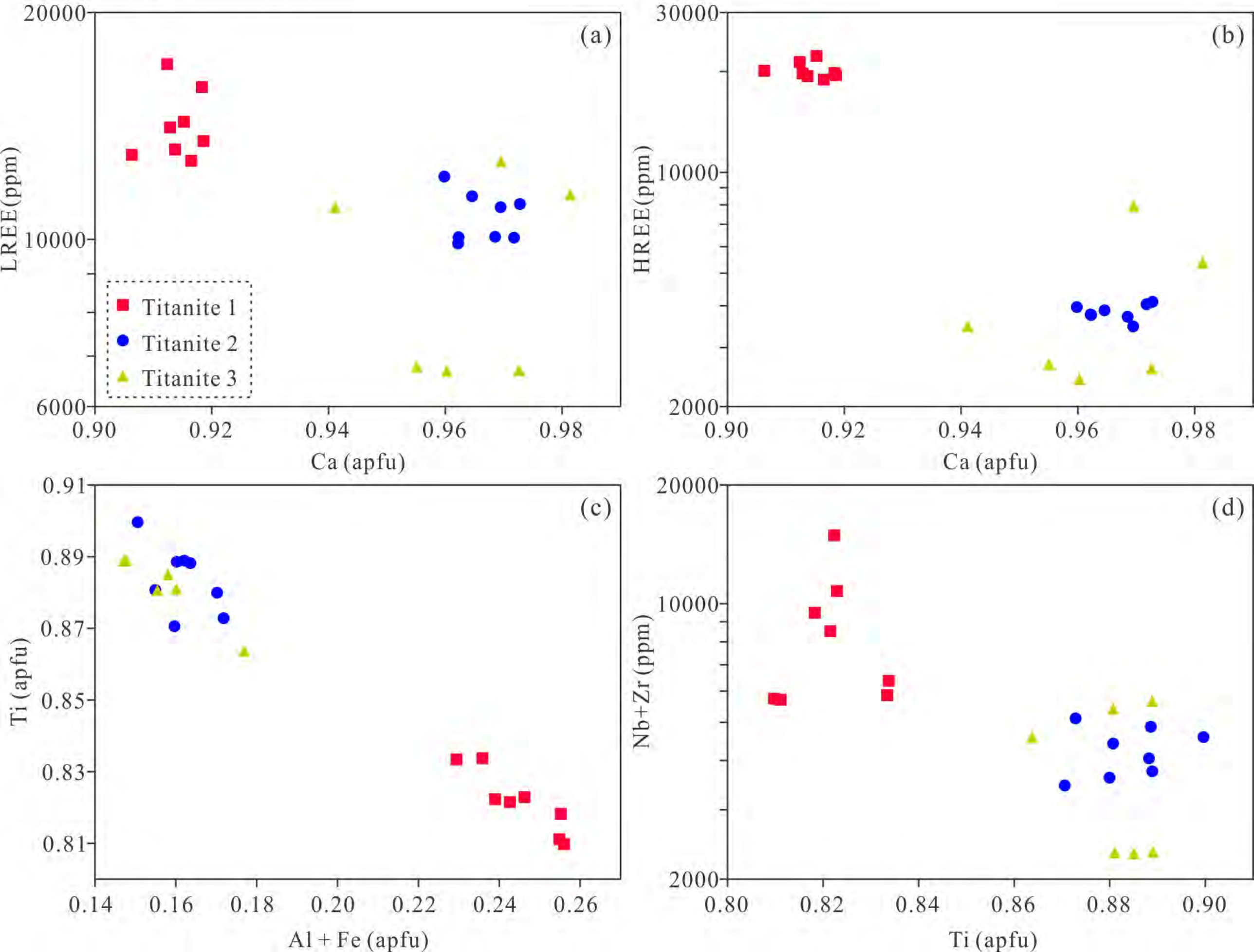
(a)
LREE(ppm)
20000
10000
6000
0.90
0.92
0.94
0.96
0.98
Ca (apfu)
Titanite 1
Titanite 2
Titanite 3
(b)
HREE(ppm)
30000
10000
2000
0.90
0.92
0.94
0.96
0.98
Ca (apfu)
(c)
Ti (apfu)
0.91
0.89
0.87
0.85
0.83
0.81
0.14
0.16
0.18
0.20
0.22
0.24
0.26
Al + Fe (apfu)
(d)
Nb+Zr (ppm)
20000
10000
2000
0.80
0.82
0.84
0.86
0.88
0.90
Ti (apfu)

Figure 11

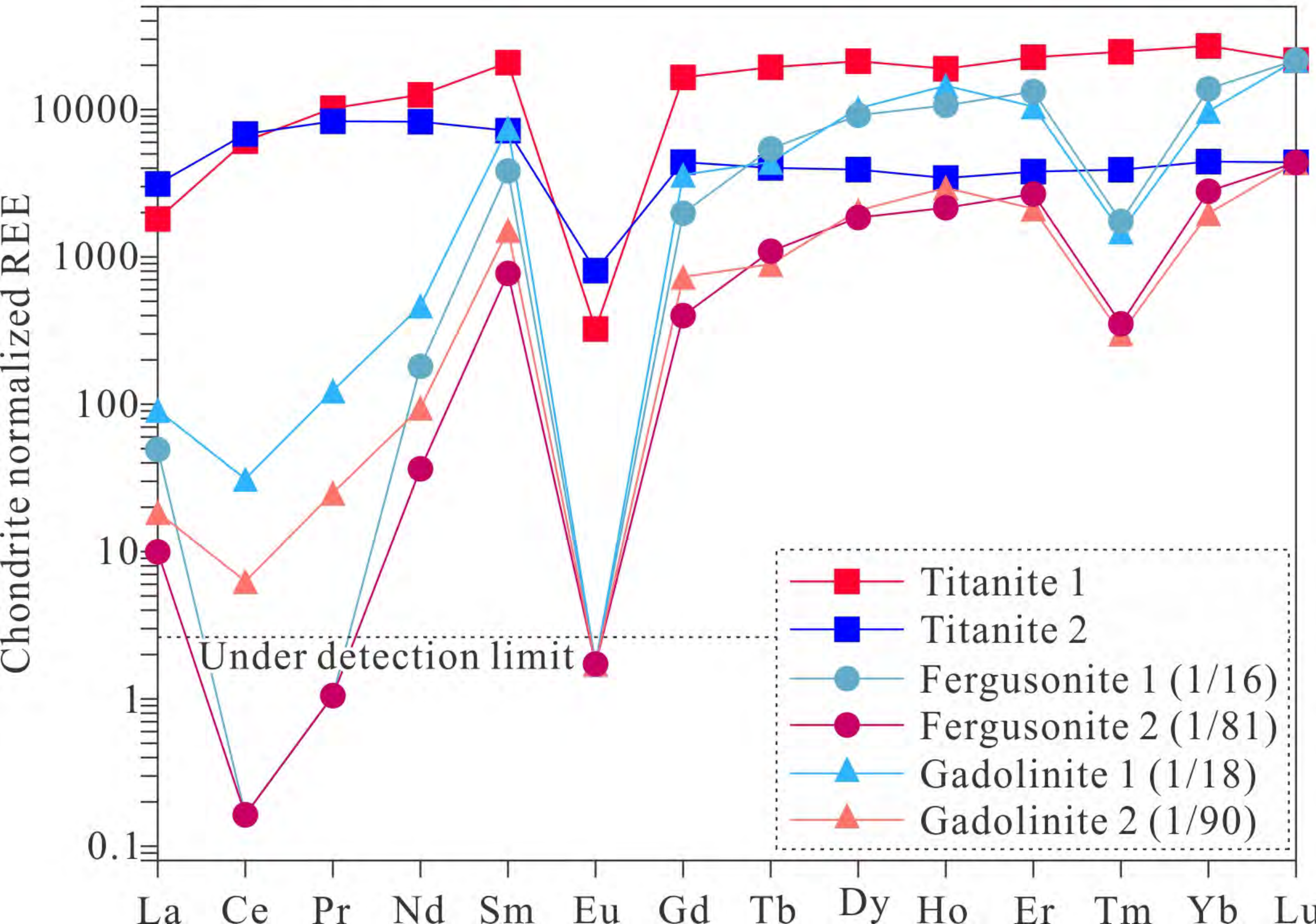
Chondrite normalized REE
10000
1000
100
10
1
0.1
Under detection limit
La
Ce
Pr
Nd
Sm
Eu
Gd
Tb
Dy
Ho
Er
Tm
Yb
Lu
Titanite 1
Titanite 2
Fergusonite 1 (1/16)
Fergusonite 2 (1/81)
Gadolinite 1 (1/18)
Gadolinite 2 (1/90)

Figure 12

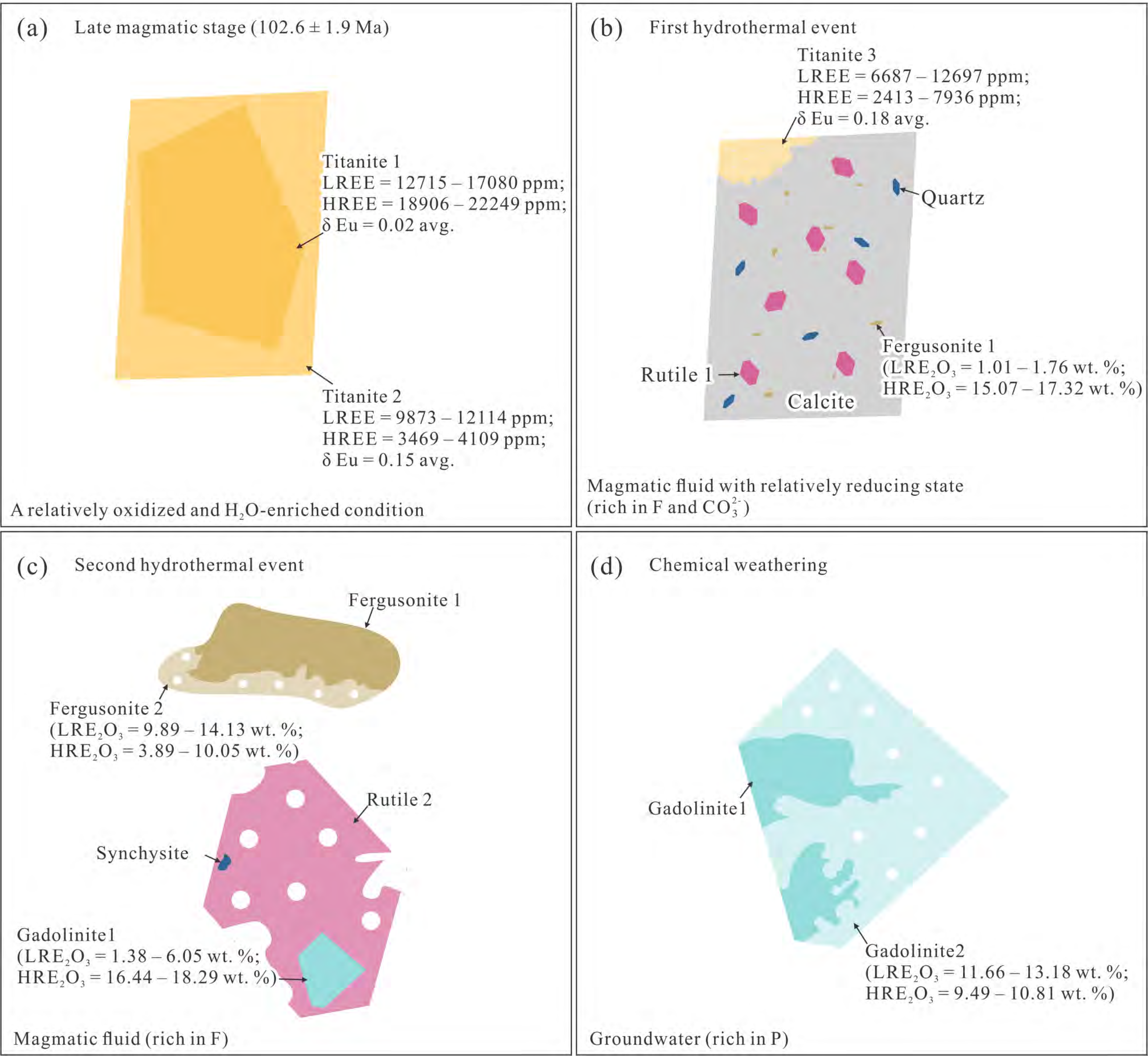
(a) Late magmatic stage (102.6 ± 1.9 Ma)
Titanite 1
LREE = 12715 – 17080 ppm;
HREE = 18906 – 22249 ppm;
δ Eu = 0.02 avg.
Titanite 2
LREE = 9873 – 12114 ppm;
HREE = 3469 – 4109 ppm;
δ Eu = 0.15 avg.
A relatively oxidized and H_2O-enriched condition
(b) First hydrothermal event
Titanite 3
LREE = 6687 – 12697 ppm;
HREE = 2413 – 7936 ppm;
δ Eu = 0.18 avg.
Quartz
Fergusonite 1
(LRE_2O_3 = 1.01 – 1.76 wt. %;
HRE_2O_3 = 15.07 – 17.32 wt. %)
Rutile 1
Calcite
Magmatic fluid with relatively reducing state
(rich in F and CO_3^{2-})
(c) Second hydrothermal event
Fergusonite 1
Fergusonite 2
(LRE_2O_3 = 9.89 – 14.13 wt. %;
HRE_2O_3 = 3.89 – 10.05 wt. %)
Rutile 2
Synchysite
Gadolinite1
(LRE_2O_3 = 1.38 – 6.05 wt. %;
HRE_2O_3 = 16.44 – 18.29 wt. %)
Magmatic fluid (rich in F)
(d) Chemical weathering
Gadolinite1
Gadolinite2
(LRE_2O_3 = 11.66 – 13.18 wt. %;
HRE_2O_3 = 9.49 – 10.81 wt. %)
Groundwater (rich in P)